# CONTRIBUTIONS
# OF THE ASTRONOMICAL OBSERVATORY
# SKALNATÉ PLESO

## • VOLUME LIII •

## Number 2

November 2023

# Editorial Board

# CONTENTS

## SOLAR SYSTEM

## GENERAL RELATIVITY

## STARS

The Contributions of the Astronomical Observatory Skalnaté Pleso
are available in a full version
in the frame of ADS Abstract Service
and can be downloaded in a usual way from the URL address:

**https://ui.adsabs.harvard.edu/**

as well as from the web-site of
the Astronomical Institute of the Slovak Academy of Sciences
on the URL address:

**https://www.astro.sk/caosp/caosp.php**

The journal is covered/indexed by:

**Web of Science (WoS)**
WoS Core Collection: Science Citation Index Expanded

**SCOPUS**

**Index Copernicus International**

# First reported observation of asteroids 2017 AB8, 2017 QX33, and 2017 RV12

**V. Troianskyi**[1,2] , **V. Kashuba**[3] , **O. Bazyey**[1,4] , **H. Okhotko**[1,3] ,

**V. Savanevych**[5] , **S. Khlamov**[6] and **A. Briukhovetskyi**[7]

[1] *Department of Physics and Astronomy FMPIT of Odesa I. I. Mechnykov National University, Pastera Street 42, 65082 Odesa, Ukraine, (E-mail: v.troianskyi@onu.edu.ua)*

[2] *Department of Physics and Methods of Teaching, Faculty of Physics and Technology, Vasyl Stefanyk Precarpathian National University, Shevchenko Street 57, 76000 Ivano-Frankivsk, Ukraine*

[3] *Astronomical Observatory of Odesa I. I. Mechnykov National University, Marazliivska 1v, 65014 Odesa, Ukraine*

[4] *Department of Mathematics, Physics and Astronomy, Odesa National Maritime University, Mechnykov Street 34, 65029 Odesa, Ukraine*

[5] *Department of Systems Engineering of Kharkiv National University of Radio Electronics, Nauki ave., 14, 61166 Kharkiv, Ukraine*

[6] *Department of Media Systems and Technologies of Kharkiv National University of Radio Electronics, Nauki ave., 14, 61166 Kharkiv, Ukraine*

[7] *Western Radio Technical Surveillance Center, State Space Agency of Ukraine, Kosmonavtiv Street, 89600 Mukachevo, Ukraine*

**Abstract.** In this paper, we show the result of the joint use of the OMT-800 telescope, the CoLiTec software, and the Väisälä method. The paper considers in detail several of the discovered (rediscovered) asteroids: 2017 AB8, 2017 QX33, and 2017 RV12 from a long list of small bodies of the Solar System.
**Key words:** Minor planets, asteroids: general – Methods: observational, numerical

## 1. Introduction

The Odesa Astronomical Observatory (OAO) has a long history of patrol observations as well as targeted observation campaigns. During the implementation of various observational programs, a large amount of scientific value information has been accumulated in the observatory archive.

Against the backdrop of constant interest in the search and study of Solar System objects, we strive to extract the maximum additional information from

the observations obtained, using the modern processing tools at our disposal. We will talk about the search for moving objects in a series of panoramic images of the starry sky, which were obtained earlier in the course of observing a particular object with the OMT-800 telescope (Andrievsky et al., 2013). The method of storage of observational information and the organization of access to it is an independent task; however, in the case of CCD images, as a rule, we conduct additional research in hot pursuit. The research resource is thousands of images with a penetrating power of up to 20 magnitude obtained during the observational season, covering tens of square degrees of the sky. At the time of writing this manuscript, the number of registered small bodies of the Solar System, according to the Minor Planet Center[1] (MPC), is almost 1.3 million and continues to grow every week, thanks to the efforts of search groups (asteroid surveys). The overwhelming majority of known small bodies belong to the main asteroid belt, and it should be expected that their number in the field of view will be greater when the field of view is close to the ecliptic zone.

OMT-800 telescope targets are often just asteroids, which increases our chances of finding and measuring other small bodies in the telescope's field of view. With the help of specialized software for searching for asteroids and comets CoLiTec (Khlamov et al., 2018) introduced at OAO in 2017, we are able to detect the trajectories of objects relative to fixed stars in the OMT-800 telescope field of view in one series of frames. Once the MPC has been identified, the detected objects may contain previously unknown objects. The search for unknown small bodies of the Solar System as an accompanying result (a byproduct) is the goal of our work.

## 2. Observations and data reduction

All the source material for our work was obtained at the OMT-800 telescope (0.8-m main mirror) during the Solar System object astrometric and photometric compaignes in 2017. The telescope was installed at the suburban observation station Astronomical Observatory of Odesa I. I. Mechnykov National University, in Mayaky village in the Odesa region, with coordinates: latitude $+46°23'49.1''$, longitude $+30°16'16.6''$ E, altitude 19 meters; and has code: 583 Odesa-Mayaky, (Kashuba et al., 2015). To obtain images of observed objects, the telescope is equipped with a FLI ML09000 camera, which, together with a field corrector, provides a field of view of $59' \times 59'$ and an image scale of 1.15 arcsec/pixel. A detailed description of the optical scheme of the telescope and additional equipment is given by Andrievsky et al. (2013).

Note that since the launch in 2012, the objects of observation on the OMT-800 telescope for astrometry and photometry have been: 1) asteroids and comets (Kleschonok et al., 2018; Troianskyi et al., 2019; Carry et al., 2021; Kwiatkowski et al., 2021; Kleshchonok et al., 2022; Oszkiewicz et al., 2020, 2021, 2023); 2)

---

[1] https://minorplanetcenter.net

artificial Earth satellites, including space debris (Bazey, 2014; Romanyuk et al., 2021); 3) variable stars (Pavlenko et al., 2019; Simon et al., 2019); and 4) stellar occultation by asteroids (Santos-Sanz et al., 2022; Rommel et al., 2023). The field of view, the penetrating ability of the telescope depending on the duration of exposure and a series of images over a time interval of more than 1 hour allow us to hope for related results. In our publication, we present the most interesting of them, since they led to the discovery of previously unknown asteroids among dozens of other numbered objects detected during the observing season.

We did standard data reduction (i.e., dark subtracting and flat-fielding); for details, see Oszkiewicz et al. (2019, 2020, 2021, 2023). After that, we used frame summation (see details in Sec. 3) to detect objects of lower magnitude (Troianskyi et al., 2014b).

## 3. CoLiTec software

The CoLiTec[2] (Collection Light Technology) software is a widely used astronomical package, which implements the different mathematical methods for the series of frames processing in real-time (Savanevych et al., 2023). This is a complex system for astronomical data processing, which includes user-friendly tools for processing control, results reviewing, integration with online catalogs, and a lot of different computational modules that are based on the developed mathematical computational methods.

The main functional features of the CoLiTec software are described below:

– working with a very wide field of view (up to 10 square degrees);

– automated calibration and cosmetic correction;

– frame summation or track-and-stack;

– brightness equalization and background alignment;

– automated rejection of the worst observations;

– fully automatic robust algorithm of astrometric and photometric reduction;

– automated objects rejection with bad or unclear measurements;

– automated detection of faint moving objects (SNR > 2.5);

– automated detection of very slow and very fast objects (from 0.7 to 40.0 pixels/frame);

– multi-threaded processing support;

---

[2] https://colitec.space

  – multi-core systems support with the ability to manage individual treatment processes;

  – processing pipeline managed by On-Line Data Analysis System (OLDAS).

More detailed information on the CoLiTec software and its comparison with other astronomical software packages is described in Savanevych et al. (2022).

## 4. Väisälä method

The Väisälä method can be extremely useful in many cases (Väisälä, 1940). It comes into wide use when you have a very short observing arc, not long enough to determine the "real" orbit and predict the object's position within the next week or so. Also, the method allows to obtain a sufficiently good primary orbit for further refinement by one of the iterative methods. This method is actively used to search for the primary orbit of small bodies of the Solar System in a short observation arc at the MPC.

### 4.1. Orbit determination

Since observations are made from the Earth, it is obvious that

$$\overrightarrow{\rho_i} = \overrightarrow{r_i} + \overrightarrow{R_i}, \tag{1}$$

where $\rho_i$ are the geocentric distances of the object, $r_i$ are the heliocentric distances of the object and $R_i$ are the geocentric distances of the Sun.

Each observation of an object gives topocentric directions to this object. After reduction to the center of the Earth, we get right ascension ($\alpha_i$) and declination ($\delta_i$) for a certain moment ($t_i$) and this allows us to write three connected equations:

$$\begin{cases} \rho_i \cos \alpha_i \cos \delta_i = x_i + X_i, \\ \rho_i \sin \alpha_i \cos \delta_i = y_i + Y_i, \\ \rho_i \sin \delta_i = z_i + Z_i, \end{cases} \tag{2}$$

where $X_i, Y_i, Z_i$ are the rectangular geocentric equatorial coordinates of the Sun and $x_i, y_i, z_i$ are the rectangular heliocentric equatorial coordinates of the object.

The geocentric coordinates of the Sun are known from any model of the Solar System, and the unknown quantities in Equations 2 are the geocentric distances ($\rho_i$) and the heliocentric coordinates ($x_i, y_i, z_i$) of the object.

### 4.2. Method

The classic Väisälä method (Gingrich, 1951) assumes that you have two observations of an object at times $t_1$ and $t_2$. A Väisälä orbit is the one that satisfies

both viewpoints and the object is on the apsidal axis at time $t_2$, at the perihelion or aphelion of its orbit. Mathematically, it looks like this:

$$\left.\frac{dr}{dt}\right|_2 = 0. \tag{3}$$

The essence of the classical Väisälä method is that we find the primary orbit from two close observations $(t_1, \alpha_1, \delta_1, t_2, \alpha_2, \delta_2)$. In this case, we choose so that the inequality is true (orbit closer to circular):

$$0 < a - r_2 < 0.5, \tag{4}$$

where $a$ is the semi-major axis of the object's orbit. After that, we write an expression for finding the geocentric rectangular coordinates of the object:

$$\begin{cases} x_2 = \Delta_2 \cos \alpha_2 + X_2, \\ y_2 = \Delta_2 \sin \alpha_2 + Y_2, \\ z_2 = \Delta_2 \tan \delta_2 + Z_2, \end{cases} \tag{5}$$

where $\Delta_2 = \rho_2 \cos \delta_2$. Thus, we found $\overrightarrow{r_2}$.

We write the geocentric velocity components in the following form:

$$\begin{cases} \dot{x}_2 = \frac{\Delta_1 \cos \alpha_1 - F_1 x_2 + X_1}{G_1}, \\ \dot{y}_2 = \frac{\Delta_1 \sin \alpha_1 - F_1 y_2 + Y_1}{G_1}, \\ \dot{z}_2 = \frac{\Delta_1 \tan \delta_1 - F_1 z_2 + Z_1}{G_1}, \end{cases} \tag{6}$$

where $\Delta_1 = \frac{F_1 r_2 + X_1 x_1 + Y_1 y_1 + Z_1 z_1}{x_2 \cos \alpha_1 + y_2 \sin \alpha_1 + z_2 \tan \delta_1}$, $F_1 = 1 - A\tau^2$, $G_1 = \tau - B\tau^3$, $A = \frac{r^3}{2}$, $B = \frac{A}{3}$, $\tau = k(t_1 - t_2)$ is the time interval between observations, and $k$ is the gravitational constant. Thus, we found $\overrightarrow{v_2}$.

The results obtained $(x_2, y_2, z_2, \dot{x}_2, \dot{y}_2, \dot{z}_2)$ can be applied to find the Keplerian elements of the object's orbit at time $t_2$.

## 5. Results

Discoverers will be defined by the MPC only when an object is numbered. At that time, the time tags on all the observations included in the solution will be examined. The discovery observation will be that observation which is the earliest-reported observation at the opposition with the earliest-reported second-night observation (M.P.E.C. 2010-U20).

The OMT-800 is one of 27 telescopes in the Gaia Follow-Up Network for Solar System Objects[3] (Gaia-FUN-SSO; Troianskyi et al. (2014a); Carry et al. (2021)). The Gaia-FUN-SSO is to coordinate ground-based observations on alert triggered by the data processing system during the mission for the confirmation

---

[3] https://gaiafunsso.imcce.fr/index.php

of newly detected moving objects or for the improvement of orbits of some critical targets. Gaia scans the sky following a predefined scanning law, and such ground-based observations are required to avoid the loss of newly detected Solar System objects and to facilitate their subsequent identification by the probe.

### 5.1. Main-belt asteroid 2017 AB8 (2014 OD380)

On 3 January 2017, we observed one of Gaia Alert (*g16347*; Tab. 1), as a result we managed to find another candidate for a discovery object (using CoLiTec software). Using the Väisälä method, we determined the preliminary orbit of the new object and then calculated its position for the next weeks. As a result, on January 26 we again observed our object, which subsequently received the name 2017 AB8 (MPS 762342).

**Table 1.** Our observations of asteroid 2017 AB8.

| Date | J2000 RA, field center | J2000 Dec, field center | Obs. object | Exp. time | Series duration | Num. of frames |
|------|------------------------|-------------------------|-------------|-----------|-----------------|----------------|
| 2017-01-03 | 09 31 25.4 | +02 44 17.3 | *g16347* | 30 sec | $1^h\ 03^{min}$ | 50 |
| 2017-01-26 | 09 14 45.1 | +01 20 27.1 | *2017 AB8* | 30 sec | $1^h\ 04^{min}$ | 60 |
| 2017-02-19 | 08 53 41.5 | +01 41 35.4 | *2017 AB8* | 30 sec | $1^h\ 25^{min}$ | 55 |

Based on our Tab. 4 and colleagues' observations from other observatories, it turned out that the asteroid 2017 AB8 (MPS 768338) is the previously lost object 2014 OD380 (MPS 525811), and was rediscovered by us.

### 5.2. Mars-crossing asteroid 2017 QX33

One of the tasks that the OMT-800 telescope performs is photometric observations. On 25 July 2017, we observed the 2014 YC15 asteroid (Troianskyi et al. (2019); Tab. 2) and, at the same time, using CoLiTec software we found a candidate for a new object in the field of view of the OMT-800 telescope.

**Table 2.** Our observations of asteroid 2017 QX33.

| Date | J2000 RA, field center | J2000 Dec, field center | Obs. object | Exp. time | Series duration | Num. of frames |
|------|------------------------|-------------------------|-------------|-----------|-----------------|----------------|
| 2017-08-25 | 23 12 11.7 | +06 19 21.5 | *2014 YC15* | 120 sec | $3^h\ 53^{min}$ | 72 |
| 2017-08-29 | 23 10 03.8 | +05 58 12.1 | *2017 QX33* | 120 sec | $0^h\ 47^{min}$ | 24 |
| 2017-09-16 | 23 03 14.0 | +02 16 20.6 | *2017 QX33* | 60 sec | $2^h\ 12^{min}$ | 50 |

Using the Väisälä method, we determined the preliminary orbit of the new object and then calculated its position for the next days. On 29 July we again observed a candidate for a new object, which as a result was named 2017 QX33 (MPS 813479). On 16 August, we again observed the 2017 QX33 asteroid with the OMT-800 telescope (MPS 81712; Tab. 5).

At the time of writing this manuscript, asteroid 2017 QX33 was listed in the MPC as: "First reported observation by Odesa-Mayaky on 2017-08-25".

### 5.3. Main-belt asteroid 2017 RV12

One of the main objects of observation at the OMT-800 telescope are artificial Earth satellites and space debris. On 14 September 2017, while observing satellite OSIRIS-REx[4], by using CoLiTec software we found another candidate for a new object in the field of view of the telescope.

**Table 3.** Our observations of asteroid 2017 RV12.

| Date | J2000 RA, field center | J2000 Dec, field center | Obs. object | Exp. time | Series duration | Num. of frames |
|------|------------------------|--------------------------|-------------|-----------|-----------------|----------------|
| 2017-09-14 | 00 22 17.7 | +02 35 15.8 | *OSIRIS-REx* | 60 sec | $2^h \ 00^{min}$ | 56 |
| 2017-09-16 | 00 19 52.0 | +02 43 03.9 | *2017 RV12* | 60 sec | $2^h \ 05^{min}$ | 50 |

Using the Väisälä method, we determined the preliminary orbit of the new object and then calculated its position for the next days. On 16 September we again observed a candidate for a new object, which as a result was named 2017 RV12 (MPS 1152157; Tab. 6).

At the time of writing this manuscript, asteroid 2017 RV12 was listed in the MPC as: "First reported observation by Odesa-Mayaky on 2017-09-14".

## 6. Summary

The CoLiTec software (Khlamov & Savanevych, 2020) is a suitable and convenient tool for identifying new small bodies in the Solar System. The Väisälä method is very stable for determining a preliminary orbit of new small bodies of the Solar System.

The combined use of the OMT-800 telescope, CoLiTec software, and the Väisälä method showed good results in the search for small bodies in the Solar System (2017 AB8, 2017 QX33, 2017 RV12).

Astrometric observations are very important for further research (numerical integration of orbits) of small bodies of the Solar System (Troianskyi & Bazyey, 2018; Troianskyi et al., 2023).

---

[4] https://www.nasa.gov/osiris-rex

**Table 4.** Our observations in MPC of asteroid 2017 AB8. Where: RA is astrometric right ascension and DEC is declination of the target center with respect to the observing site (Location); Mag. - asteroid approximate magnitude and references (Ref.) in Minor Planet Electronic Circulars.

| Date (UT) | J2000 RA | J2000 Dec | Mag. | Location | Ref. |
|---|---|---|---|---|---|
| 2017 01 03.96407 | 09 31 25.01 | +02 48 39.6 | 20.2 | Odesa-Mayaky | MPS 757613 |
| 2017 01 04.00278 | 09 31 23.90 | +02 48 27.2 | 19.5 | Odesa-Mayaky | MPS 757613 |
| 2017 01 04.02108 | 09 31 23.38 | +02 48 20.1 | 20.1 | Odesa-Mayaky | MPS 757613 |
| 2017 01 04.04478 | 09 31 22.71 | +02 48 11.9 | 19.1 | Odesa-Mayaky | MPS 757613 |
| 2017 01 26.94419 | 09 15 09.20 | +01 28 04.4 | 19.4 | Odesa-Mayaky | MPS 762342 |
| 2017 01 26.95308 | 09 15 08.76 | +01 28 04.8 | 19.0 | Odesa-Mayaky | MPS 767286 |
| 2017 01 26.95556 | 09 15 08.57 | +01 28 03.5 | 20.1 | Odesa-Mayaky | MPS 762342 |
| 2017 01 26.96395 | 09 15 08.14 | +01 28 02.0 | 19.4 | Odesa-Mayaky | MPS 762342 |
| 2017 01 26.96641 | 09 15 07.98 | +01 28 01.6 | 20.4 | Odesa-Mayaky | MPS 762342 |
| 2017 01 26.97541 | 09 15 07.46 | +01 28 02.3 | 18.6 | Odesa-Mayaky | MPS 767286 |
| 2017 01 26.97792 | 09 15 07.31 | +01 28 01.2 | 18.7 | Odesa-Mayaky | MPS 767286 |
| 2017 01 26.98663 | 09 15 06.86 | +01 28 00.5 | 19.1 | Odesa-Mayaky | MPS 762342 |
| 2017 01 26.98914 | 09 15 06.71 | +01 28 00.4 | 19.1 | Odesa-Mayaky | MPS 762342 |
| 2017 02 19.84208 | 08 53 19.87 | +01 41 33.1 | 19.3 | Odesa-Mayaky | MPS 768338 |
| 2017 02 19.85598 | 08 53 19.20 | +01 41 34.8 | 19.3 | Odesa-Mayaky | MPS 768338 |
| 2017 02 19.86955 | 08 53 18.48 | +01 41 37.2 | 19.7 | Odesa-Mayaky | MPS 768338 |
| 2017 02 19.88564 | 08 53 17.68 | +01 41 39.5 | 19.0 | Odesa-Mayaky | MPS 768338 |

**Table 5.** Our observations in MPC of asteroid 2017 QX33. Where: RA is astrometric right ascension and DEC is declination of the target center with respect to the observing site (Location); Mag. - asteroid approximate magnitude and references (Ref.) in Minor Planet Electronic Circulars.

| Date (UT) | J2000 RA | J2000 Dec | Mag. | Location | Ref. |
|---|---|---|---|---|---|
| 2017 08 25.90477 | 23 11 03.83 | +06 26 26.1 | 19.2 | Odesa-Mayaky | MPS 813479 |
| 2017 08 25.91872 | 23 11 03.64 | +06 26 20.5 | 18.9 | Odesa-Mayaky | MPS 813479 |
| 2017 08 25.93113 | 23 11 03.41 | +06 26 15.2 | 19.7 | Odesa-Mayaky | MPS 813479 |
| 2017 08 30.01831 | 23 09 54.28 | +05 51 57.4 | 18.9 | Odesa-Mayaky | MPS 813479 |
| 2017 08 30.03580 | 23 09 53.83 | +05 51 46.6 | 19.3 | Odesa-Mayaky | MPS 813479 |
| 2017 08 30.05153 | 23 09 53.49 | +05 51 38.6 | 19.3 | Odesa-Mayaky | MPS 813479 |
| 2017 09 16.85311 | 23 03 14.03 | +02 16 20.6 | 18.7 | Odesa-Mayaky | MPS 817121 |
| 2017 09 16.87280 | 23 03 13.54 | +02 16 04.1 | 18.7 | Odesa-Mayaky | MPS 817121 |
| 2017 09 16.90047 | 23 03 12.84 | +02 15 40.9 | 18.7 | Odesa-Mayaky | MPS 817121 |
| 2017 09 16.91976 | 23 03 12.33 | +02 15 24.3 | 18.7 | Odesa-Mayaky | MPS 817121 |

**Table 6.** Our observations in MPC of asteroid 2017 RV12. Where: RA is astrometric right ascension and DEC is declination of the target center with respect to the observing site (Location); Mag. - asteroid approximate magnitude and references (Ref.) in Minor Planet Electronic Circulars.

| Date (UT) | J2000 RA | J2000 Dec | Mag. | Location | Ref. |
|---|---|---|---|---|---|
| 2017 09 14.87524 | 00 21 11.04 | +02 54 14.1 | 19.8 | Odesa-Mayaky | MPS 817137 |
| 2017 09 14.88859 | 00 21 10.48 | +02 54 10.1 | 21.0 | Odesa-Mayaky | MPS 817137 |
| 2017 09 14.90273 | 00 21 09.87 | +02 54 05.2 | 20.4 | Odesa-Mayaky | MPS 817137 |
| 2017 09 14.91764 | 00 21 09.24 | +02 53 59.9 | 20.9 | Odesa-Mayaky | MPS 817137 |
| 2017 09 14.93109 | 00 21 08.75 | +02 53 55.7 | 21.3 | Odesa-Mayaky | MPS 817137 |
| 2017 09 16.80051 | 00 19 53.72 | +02 43 05.4 | 20.0 | Odesa-Mayaky | MPS 1152157 |
| 2017 09 16.81462 | 00 19 53.15 | +02 43 00.7 | 19.5 | Odesa-Mayaky | MPS 1152157 |
| 2017 09 16.84238 | 00 19 51.90 | +02 42 50.4 | 19.6 | Odesa-Mayaky | MPS 1152157 |
| 2017 09 16.86374 | 00 19 50.95 | +02 42 43.1 | 19.9 | Odesa-Mayaky | MPS 1152157 |
| 2017 09 16.88714 | 00 19 49.90 | +02 42 34.5 | 19.8 | Odesa-Mayaky | MPS 1152157 |

# References

Andrievsky, S. M., Fashchevsky, N. N., Podlesnyak, S. V., et al., A New 800 mm Automatic Telescope. 2013, *Odessa Astronomical Publ.*, **26**, 6

Bazyey, A. A., The Simulation of the Orbital Evolution of a Passive High-Orbit Fragment with Large Surface Area. 2014, *Odessa Astronomical Publ.*, **27**, 108, DOI: 10.48550/arXiv.1404.4570

Carry, B., Thuillot, W., Spoto, F., et al., Potential asteroid discoveries by the ESA Gaia mission. Results from follow-up observations. 2021, *Astronomy and Astrophysics*, **648**, A96, DOI: 10.1051/0004-6361/202039579

Gingrich, C. H., Book Review: Formulae and Directions for Computing the Orbits of Minor Planets and Comets, by Y. Väisälä and L. Oterma. 1951, *Popular Astronomy*, **59**, 396

Kashuba, S. G., Gorbanev, Y. M., Andrievsky, S. M., Marsakova, V. I., & Troianskyi, V. V., The Quantity and Quality of Observational Nights Monitored with Using the Astronomical Instruments at the Suburban Observation Stations of Astronomical Observatory of Odessa National University. 2015, *Odessa Astronomical Publ.*, **28**, 16

Khlamov, S. & Savanevych, V. 2020, *Big Astronomical Datasets and Discovery of New Celestial Bodies in the Solar System in Automated Mode by the CoLiTec Software* (Elsevier), 331  345

Khlamov, S., Savanevych, V., Briukhovetskyi, O., et al., CoLiTec Software for the Astronomical Data Sets Processing. 2018, *Proceedings of the 2018 IEEE 2nd International Conference on Data Stream Mining and Processing, DSMP 2018*, 227 230, DOI: 10.1109/DSMP.2018.8478504

Kleschonok, V. V., Luk'yanyk, I. V., Gorbanev, Y. M., & Kashuba, V. I., Photometric study of the C/2014 Q2 (Lovejoy) comet plasma tails. 2018, *Planetary Space Science*, **164**, 1, DOI: 10.1016/j.pss.2018.04.007

Kleshchonok, V. V., Kashuba, V. I., Andrievsky, S. M., & Gorbanev, Y. M., Surface structure and assessment of dust productivity of the cometary nucleus C/2017 K2 (PANSTARRS). 2022, *Mathematical Modeling and Computing*, **9**, 159, DOI: 10.23939/mmc2022.01.159

Kwiatkowski, T., Koleńczuk, P., Kryszczyńska, A., et al., Photometry and model of near-Earth asteroid 2021 DW1 from one apparition. 2021, *Astronomy and Astrophysics*, **656**, A126, DOI: 10.1051/0004-6361/202142013

Oszkiewicz, D., Kryszczyska, A., Kankiewicz, P., et al., Physical and dynamical properties of the unusual V-type asteroid (2579) Spartacus. 2019, *Astronomy and Astrophysics*, **623**, A170, DOI: 10.1051/0004-6361/201833641

Oszkiewicz, D., Troianskyi, V., Föhring, D., et al., Spin rates of V-type asteroids. 2020, *Astronomy and Astrophysics*, **643**, A117, DOI: 10.1051/0004-6361/202038062

Oszkiewicz, D., Troianskyi, V., Galad, A., et al., Spins and shapes of basaltic asteroids in the inner Main Belt and the missing dunite problem. 2023, *Icarus*, **397**, id. 115520, DOI: 10.1016/j.icarus.2023.115520

Oszkiewicz, D., Wilawer, E., Podlewska-Gaca, E., et al., First survey of phase curves of V-type asteroids. 2021, *Icarus*, **357**, 114158, DOI: 10.1016/j.icarus.2020.114158

Pavlenko, E., Niijima, K., Mason, P., et al., ASASSN-18fk: A new WZ Sge-type dwarf nova with multiple rebrightenings and a new candidate for a superhumping intermediate polar. 2019, *Contrib. Astron. Obs. Skalnaté Pleso*, **49**, 204, DOI: 10.48550/arXiv.1907.00623

Romanyuk, Y. O., Shulga, O. V., Shakun, L. S., et al., Monitoring the Artificial Space Objects with Ukrainian Network of Optical Stations. 2021, *Odessa Astronomical Publ.*, **34**, 85, DOI: 10.18524/1810-4215.2021.34.244926

Rommel, F. L., Braga-Ribas, F., Ortiz, J. L., et al., A large topographic feature on the surface of the trans-Neptunian object (307261) 2002 MS$_4$ measured from stellar occultations. 2023, *arXiv e-prints*, arXiv:2308.08062, DOI: 10.48550/arXiv.2308.08062

Santos-Sanz, P., Ortiz, J. L., Sicardy, B., et al., Physical properties of the trans-Neptunian object (38628) Huya from a multi-chord stellar occultation. 2022, *Astronomy and Astrophysics*, **664**, A130, DOI: 10.1051/0004-6361/202141546

Savanevych, V., Khlamov, S., Akhmetov, V., et al., CoLiTecVS software for the automated reduction of photometric observations in CCD-frames. 2022, *Astronomy and Computing*, **40**, DOI: 10.1016/j.ascom.2022.100605

Savanevych, V., Khlamov, S., Briukhovetskyi, O., Trunova, T., & Tabakova, I., Mathematical Methods for an Accurate Navigation of the Robotic Telescopes. 2023, *Mathematics*, **11**, DOI: 10.3390/math11102246

Simon, A., Pavlenko, E., Shugarov, S., et al., Gaia18aak is a new SU UMa-type dwarf nova. 2019, *Contrib. Astron. Obs. Skalnaté Pleso*, **49**, 420

Troianskyi, V., Bazey, A. A., Kashuba, V. I., & Zhukov, V. V., Determination of the small Solar system bodies orbital elements from astrometric observations with OMT-800 telescope. 2014a, in *Gaia-FUN-SSO-3*, 127–130

Troianskyi, V., Kankiewicz, P., & Oszkiewicz, D., Dynamical evolution of basaltic asteroids outside the Vesta family in the inner main belt. 2023, *Astronomy and Astrophysics*, **672**, A97, DOI: 10.1051/0004-6361/202245678

Troianskyi, V., Kashuba, V., & Krugly, Y., Photometry of Selected Asteroids on the OMT-800 Telescope. 2019, *Minor Planet Bulletin*, **46**, 109

Troianskyi, V. V., Bazyey, A. A., Kashuba, V. I., Zhukov, V. V., & Korzhavin, S. A., Method for Calculating Orbits of Near-Earth Asteroids Observed with Telescope OMT-800. 2014b, *Odessa Astronomical Publ.*, **27**, 154

Troianskyi, V. V. & Bazyey, O. A., Numerical simulation of asteroid system dynamics. 2018, *Contrib. Astron. Obs. Skalnaté Pleso*, **48**, 356

Väisälä, Y., Beobachtungen von Kleinen Planeten. 1940, *Astronomische Nachrichten*, **271**, 35, DOI: 10.1002/asna.19402710112

# Component $x$ of the gravitational acceleration in general relativity and concept of mass

## L. Neslušan[ID]

*Astronomical Institute of the Slovak Academy of Sciences*
*059 60 Tatranská Lomnica, The Slovak Republic, (E-mail: ne@ta3.sk)*

**Abstract.** In general relativity, the acceleration of a test particle in the vicinity of a massive object should be calculated by using the equation of geodesic. The specific formula for the acceleration is, however, well-known only in the Schwarzschild coordinates. Here, we present this formula in the frame with the spatial part identical to the common rectangular coordinate frame. The orientation of the acceleration and identification of physical quantities with the general integration constants can better be discerned in the latter. We emphasize that the gravitational acceleration in general relativity, for system of particles being in rest, consists of two terms. The first term is identical with the acceleration derived on the basis of Newton's gravitational law. The second term, having a smaller size above the event horizon, is a repulsive contribution to the total, attractive, gravity. The relativistic formula implies that the gravity should be repulsive below the event horizon, because the second term dominates in this region.

**Key words:** gravitational acceleration – general relativity – $x$-$y$-$z$ coordinate frame – repulsive contribution to gravity

## 1. Introduction

In Einstein's theory of general relativity (Einstein, 1915, 1916), the gravitational acceleration of a test particle (TP, hereafter) in the vicinity of other, massive, particle (MP) is given by the equation of geodesic (EoG). To calculate the acceleration, it is necessary to know the metrics of space-time generated by the MP in which the TP is situated. When the MP is a point-like particle, the outer Schwarzschild metrics (OSM) (Schwarzschild, 1916) is relevant.

The metric tensor characterizing the OSM is well known in the Schwarzschild coordinate system $O(r, \vartheta, \varphi, ct)$ ($t$ is time and $c$ is the speed of light in vacuum), i.e. with the spatial part identical with the common spherical coordinate system $O(r, \vartheta, \varphi)$. The components of the metric tensor enable us to calculate the size of the acceleration in the frame with the origin identical with the position of the point-like MP. Namely, the acceleration depends only on the $g_{rr}$ and $g_{tt}$ components of metric tensor, which both depend only on the radial distance from the MP, $r$.

However, sometimes we need to calculate the acceleration in a specific direction, in which its orientation is seen better than in the spherical coordinate frame. In this work, we derive the formula for the acceleration in the coordinate frame $\mathrm{O}(x,y,z,\tau)$, i.e. the frame with the spatial part identical with the rectangular coordinate frame $\mathrm{O}(x,y,z)$. We denoted $\tau = ct$. The general formula would be very large and, thus, difficult. Because of this reason, we adopt the assumption reducing the formula: we deal with the case when both MP and TP are in rest and, moreover, the MP is situated in the origin of the $\mathrm{O}(x,y,z)$ frame.

In the Euclidean geometry, the transformation between the spherical and rectangular coordinates is trivial. However, one can doubt if this is also valid in a curved space-time of general relativity. In this paper, we explicitly make the transformation. Although it does not give us any new result, the demonstration of how the transformation can be performed might be useful. Perhaps, it can also serve as an exercise in teaching, in a basic course on general relativity.

Beside the explicit derivation of the transformation, we are interested in a comparison between the relativistic and Newtonian formulas for the gravitational acceleration, since this comparison can help us to understand a relation between the integration constants in the Schwarzschild solution of the field equations and mass.

## 2. Transformation of coordinate frames

The coordinates in the common spherical frame, $\mathrm{O}(r, \vartheta, \varphi)$, are related to their counterparts in the rectangular frame, $\mathrm{O}(x,y,z)$, as

$$x = r \cos\varphi \sin\vartheta, \tag{1}$$

$$y = r \sin\varphi \sin\vartheta, \tag{2}$$

$$z = r \cos\vartheta. \tag{3}$$

Based on these relations, the transformation relations from $\mathrm{O}(r, \vartheta, \varphi)$ to $\mathrm{O}(x,y,z)$ are

$$r = \sqrt{x^2 + y^2 + z^2}, \tag{4}$$

$$\sin\vartheta = \sqrt{\frac{x^2 + y^2}{x^2 + y^2 + z^2}}, \qquad \cos\vartheta = \frac{z}{\sqrt{x^2 + y^2 + z^2}}, \tag{5}$$

$$\sin\varphi = \frac{y}{\sqrt{x^2 + y^2}}, \qquad \cos\varphi = \frac{x}{\sqrt{x^2 + y^2}}. \tag{6}$$

In view of the calculation of derivatives of these coordinates, it is more useful to consider the relations

$$\tan\vartheta = \frac{\sqrt{x^2 + y^2}}{z}, \tag{7}$$

$$\tan\varphi = \frac{y}{x}, \tag{8}$$

or
$$\vartheta = \arctan \frac{\rho}{z}, \tag{9}$$

$$\varphi = \arctan \frac{y}{x}. \tag{10}$$

In relation (9), we used denotation

$$\rho = \sqrt{x^2 + y^2}. \tag{11}$$

Further, we also denote

$$R = \sqrt{x^2 + y^2 + z^2}. \tag{12}$$

Although $r = R$ formally symbol $R$ is not a variable; it is only a denotation of the square root of the sum of $x$, $y$, and $z$, all squared.

One can easily find that the partial derivatives of the spherical coordinates in respect to their rectangular counterparts are

$$\frac{\partial r}{\partial x} = \frac{x}{R}, \tag{13}$$

$$\frac{\partial \vartheta}{\partial x} = \frac{xz}{R^2 \rho}, \tag{14}$$

$$\frac{\partial \varphi}{\partial x} = -\frac{y}{\rho^2}, \tag{15}$$

$$\frac{\partial r}{\partial y} = \frac{y}{R}, \tag{16}$$

$$\frac{\partial \vartheta}{\partial y} = \frac{yz}{R^2 \rho}, \tag{17}$$

$$\frac{\partial \varphi}{\partial y} = \frac{x}{\rho^2}, \tag{18}$$

$$\frac{\partial r}{\partial z} = \frac{z}{R}, \tag{19}$$

$$\frac{\partial \vartheta}{\partial z} = -\frac{\rho}{R^2}, \tag{20}$$

$$\frac{\partial \varphi}{\partial z} = 0. \tag{21}$$

If we assume both TP and MP being in rest, then

$$\frac{\partial t}{\partial x} = 0, \tag{22}$$

$$\frac{\partial t}{\partial y} = 0, \tag{23}$$

$$\frac{\partial t}{\partial z} = 0, \tag{24}$$

$$\frac{\partial (ct)}{\partial \tau} = 1. \tag{25}$$

In the Schwarzschild coordinates with the spatial part being the spherical coordinates, only the diagonal components of the metric tensor are non-zero, i.e.

$$g_{\mu\nu} = \begin{pmatrix} g_{11} & 0 & 0 & 0 \\ 0 & g_{22} & 0 & 0 \\ 0 & 0 & g_{33} & 0 \\ 0 & 0 & 0 & g_{44} \end{pmatrix} \equiv \begin{pmatrix} g_{rr} & 0 & 0 & 0 \\ 0 & g_{\vartheta\vartheta} & 0 & 0 \\ 0 & 0 & g_{\varphi\varphi} & 0 \\ 0 & 0 & 0 & g_{tt} \end{pmatrix}. \tag{26}$$

This tensor can be transformed to its counterpart in the O($x,y,z,\tau$) coordinate frame by using a well-known transformation formula

$$g_{\mu\nu} = \frac{\partial x^\alpha}{\partial x^\mu} \frac{\partial x^\beta}{\partial x^\nu} g_{\alpha\beta}. \tag{27}$$

The result of the transformation is given in Appendix A.

## 3. $x$-component of acceleration

As we mentioned in Sect. 1, we consider two particles, TP and MP. The MP is situated in the origin of the coordinate frame. The acceleration of the TP at distance $x$ from the MP is given by the EoG,

$$\frac{d^2 x^\alpha}{ds^2} + \Gamma^\alpha_{\beta\gamma} \frac{dx^\beta}{ds} \frac{dx^\gamma}{ds} = 0, \tag{28}$$

where $\Gamma^\alpha_{\beta\gamma}$ are the Christoffel symbols and $ds$ is the line element in the four-dimensional space-time. Two Christoffel symbols, which are necessary for our calculation of the $x$-component of the acceleration, are calculated in Appendix C.

With the help of the obvious equality

$$\frac{dx^\alpha}{ds} = \frac{dx^\alpha}{dt} \frac{dt}{ds}, \tag{29}$$

we can calculate the second derivative of $x^\alpha$ in respect to $s$. Specifically (Straumann, 2013, p. 59),

$$\frac{d^2 x^\alpha}{ds^2} = \frac{d}{ds} \left( \frac{dx^\alpha}{dt} \frac{dt}{ds} \right) = \left[ \frac{d}{ds} \left( \frac{dx^\alpha}{dt} \right) \right] \frac{dt}{ds} + \frac{dx^\alpha}{dt} \frac{d^2 t}{ds^2} = \frac{d^2 x^\alpha}{dt^2} \left( \frac{dt}{ds} \right)^2 + \frac{dx^\alpha}{dt} \frac{d^2 t}{ds^2}. \tag{30}$$

The second derivative $d^2t/ds^2$, occurring in relation (30), can be calculated by using EoG (28) and relation (29) as

$$\frac{d^2 t}{ds^2} \equiv \frac{d^2 x^4}{ds^2} = -\Gamma^4_{\beta\gamma} \frac{dx^\beta}{dt} \frac{dt}{ds} \frac{dx^\gamma}{dt} \frac{dt}{ds}. \tag{31}$$

Now, we can calculate the acceleration $d^2x/dt^2$. Identifying $x = x^1$, we obtain

$$\frac{d^2 x^1}{ds^2} = -\Gamma^1_{\alpha\beta} \frac{dx^\beta}{ds} \frac{dx^\gamma}{ds} \tag{32}$$

from EoG (28). Supplying relations (30) and (29) into the left-hand and right-hand sides of the last equation, respectively, this equation acquires the form

$$\frac{d^2x^1}{dt^2}\left(\frac{dt}{ds}\right)^2 + \frac{dx^1}{dt}\left(-\Gamma^4_{\beta\gamma}\frac{dx^\beta}{dt}\frac{dt}{ds}\frac{dx^\gamma}{dt}\frac{dt}{ds}\right) = -\Gamma^1_{\beta\gamma}\frac{dx^\beta}{dt}\frac{dt}{ds}\frac{dx^\gamma}{dt}\frac{dt}{ds}. \qquad (33)$$

Further, if it is divided by $(dt/ds)^2$ and the terms are re-arranged, the $x$-component of acceleration becomes

$$\frac{d^2x^1}{dt^2} = \left(\Gamma^4_{\beta\gamma}\frac{dx^1}{dt} - \Gamma^1_{\beta\gamma}\right)\frac{dx^\beta}{dt}\frac{dx^\gamma}{dt}. \qquad (34)$$

For the system of TP and MP in rest, $dx^1/dt \equiv dx/dt = 0$, $dx^2/dt \equiv dy/dt = 0$, $dx^3/dt \equiv dz/dt = 0$, and

$$\frac{dx^4}{dt} \equiv \frac{d\tau}{dt} = \frac{d(ct)}{dt} = c. \qquad (35)$$

When we also take into account relation (C17) derived in Appendix C, relation (34) is reduced to

$$\frac{d^2x^1}{dt^2} \equiv \frac{d^2x}{dt^2} = -c^2\Gamma^x_{\tau\tau} = \frac{c^2}{2}\left(g^{xx}\frac{\partial g_{\tau\tau}}{\partial x} + g^{xy}\frac{\partial g_{\tau\tau}}{\partial y} + g^{xz}\frac{\partial g_{\tau\tau}}{\partial z}\right). \qquad (36)$$

The contravariant components of the metric tensor in this relation are given by relations (B40)$-$(B42) derived in Appendix B. With the help of them, the acceleration can be given more explicitly as

$$\frac{d^2x}{dt^2} = \frac{c^2}{2}\left\{\left[\frac{x^2}{R^2}\left(1 + \frac{1}{g_{rr}}\right) - 1\right]\frac{\partial g_{\tau\tau}}{\partial x} + \frac{xy}{R^2}\left(1 + \frac{1}{g_{rr}}\right)\frac{\partial g_{\tau\tau}}{\partial y} + \right.$$
$$\left. + \frac{xz}{R^2}\left(1 + \frac{1}{g_{rr}}\right)\frac{\partial g_{\tau\tau}}{\partial z}\right\}. \qquad (37)$$

We assume that both TP and MP are situated in vacuum, therefore the metrics generated by the MP is the OSM. It is characterized by the metric tensor

$$g_{\mu\nu} = \begin{pmatrix} g_{rr} & 0 & 0 & 0 \\ 0 & g_{\vartheta\vartheta} & 0 & 0 \\ 0 & 0 & g_{\varphi\varphi} & 0 \\ 0 & 0 & 0 & g_{\tau\tau} \end{pmatrix} =$$
$$= \begin{pmatrix} -\left(1 - \frac{2L}{r}\right)^{-1} & 0 & 0 & 0 \\ 0 & -r^2 & 0 & 0 \\ 0 & 0 & -r^2\sin^2\vartheta & 0 \\ 0 & 0 & 0 & Kc^2\left(1 - \frac{2L}{r}\right) \end{pmatrix} \qquad (38)$$

Symbols $K$ and $L$ stand for the constants.

In this metrics, the derivatives of component $g_{\tau\tau}$ in respect to spatial coordinates $x$, $y$, and $z$ are

$$\frac{\partial g_{\tau\tau}}{\partial x} = K\frac{2L}{R^3}x, \tag{39}$$

$$\frac{\partial g_{\tau\tau}}{\partial y} = K\frac{2L}{R^3}y, \tag{40}$$

$$\frac{\partial g_{\tau\tau}}{\partial z} = K\frac{2L}{R^3}z, \tag{41}$$

$$\tag{42}$$

therefore formula (37) can further be simplified to

$$\frac{d^2x}{dt^2} = \frac{Kc^2L}{R^3}\left\{\left[\frac{x^2}{R^2}\left(1+\frac{1}{g_{rr}}\right)-1\right]x + \frac{xy^2}{R^2}\left(1+\frac{1}{g_{rr}}\right)+\right.$$
$$\left.+\frac{xz^2}{R^2}\left(1+\frac{1}{g_{rr}}\right)\right\} = \frac{Kc^2L}{R^3}\left[\frac{x^2+y^2+z^2}{R^2}\left(1+\frac{1}{g_{rr}}\right)x - x\right]. \tag{43}$$

Or, after a further handling with this relation, we can obtain

$$\frac{d^2x}{dt^2} = \frac{Kc^2L}{R^3 g_{rr}}x. \tag{44}$$

When the $g_{rr}$ component in the OSM is also expressed explicitly (see relation (38)) the formula for the acceleration in the direction of the coordinate axis $x$ is

$$\frac{d^2x}{dt^2} = -\left(1-\frac{2L}{R}\right)\frac{Kc^2L}{R^3}x. \tag{45}$$

(The formulas for the remaining spatial components of the acceleration, in $y$ and $z$ directions, can simply be obtained by doing the cyclic interchange of variables: $x \rightarrow y \rightarrow z \rightarrow x$.)

When the TP is situated on the coordinate $x$-axis, i.e. the components $y$ and $z$ of its radius vector are zero, then $R = \sqrt{x^2+0+0} = |x|$ and

$$\frac{d^2x}{dt^2} = -\left(1-\frac{2L}{|x|}\right)\frac{c^2KL}{x^2}\frac{x}{|x|}. \tag{46}$$

## 4. Calibration of constants and discussion

Our final formula (45), giving the acceleration of TP in the direction of the coordinate $x$-axis, can be applied to real objects if the constants $K$ and $L$ are determined. Constant $K$ used to be chosen to equal unity. We have kept this constant explicitly up to this point because there are some solutions of the field equations requiring $K \neq 1$.

Let us now establish a new constant, $M$, defined by the relation

$$L = \frac{GM}{c^2}, \tag{47}$$

where $G$ is the Newton gravitational constant. With the help of the new constant and putting $K = 1$, formula (45) can be re-written as

$$\frac{d^2x}{dt^2} = -\left(1 - \frac{2GM}{c^2R}\right)\frac{GM}{R^2}\frac{x}{R}. \tag{48}$$
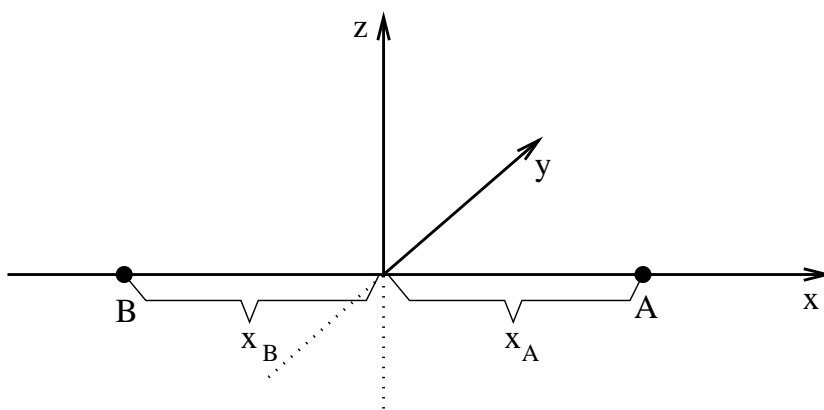


**Figure 1.** The positions, A and B, of the test particle (TP) in the field of a massive, point-like particle, which is placed in the origin of the rectangular coordinate frame. Notice that $x > 0$ at position A, but $x < 0$ at position B.

In the limit of weak gravitational field, i.e. when $2GM/(c^2R) \ll 1$, the last formula is reduced to its counterpart in the Newtonian physics,

$$\frac{d^2x}{dt^2} = -\frac{GM}{x^2}\frac{x}{R}. \tag{49}$$

with $M$ being the mass of the MP. We can see that it correctly determines the orientation of the acceleration. This is clear when we consider two positions of the TP, A and B, on the coordinate $x$-axis shown in Fig. 1. If the TP is at position A, then its $x$ coordinate $x_A > 0$. Hence, $x_A = |x_A|$ and the acceleration $d^2x/dt^2 = -GM/|x_A|^2 < 0$. This means, it is oriented in the opposite direction in respect to the orientation of the coordinate $x$-axis. If the TP is at position B, then $x_B < 0$ and $x_B = -|x_B|$. This implies that the acceleration $d^2x/dt^2 = +GM/|x_B|^2 > 0$. Its orientation is the same as the orientation of the $x$-axis. Thus, seeing Fig. 1, the TP is attracted toward the MP at both positions.

Let us return to the relativistic formula (48). We see that the acceleration is expressed by two terms, explicitly

$$\frac{d^2x}{dt^2} = -\frac{GM}{R^2}\frac{x}{R} + \frac{2G^2M^2}{c^2R^4}x. \qquad (50)$$

Notice that the sign of the second, relativistic, term is opposite to the first, Newtonian, term. In other words, the first (second) term is negative (positive) when $x > 0$ and vice versa when $x < 0$. The relativistic term reduces the Newtonian term above the event horizon, i.e. when $2GM/(c^2R) < 1$. When the gravitational acceleration in this region is calculated (i) using the relativistic formula (48) and (ii) the Newtonian formula (49), then the relativistic acceleration is smaller than its Newtonian counterpart.

The relativistic term of acceleration can be understood as a repulsive contribution to the attractive Newtonian acceleration. There have been published solutions of the field equations to model the relativistic compact objects, which implied an outward oriented gravitational attraction in the innermost region of the objects (Ni, 2011; Neslušan, 2015, 2017a,b, 2019; deLyra, 2021; Neslušan, 2022; deLyra & Carneiro, 2023; deLyra et al., 2023). Since the relativistic term is proportional to the mass of MP squared, there can occur a distribution of matter where the relativistic term dominates even above the event horizon (e.g. Neslušan, 2019, Sect. 3). When we take into account this possibility, the outward oriented gravitational attraction in the innermost region of compact objects, according to some models of these, is not surprising.

The relativistic term clearly dominates below the event horizon, i.e. in the regime of gravity with $2GM/(c^2R) > 1$ according to the derived formulas. This means that a TP is repelled from a massive object (black hole?) in this region.

## 5. Conclusion

The orientation of the gravitational attraction within general relativity is more transparent in the O($x$,$y$,$z$,$ct$) coordinate frame than in the Schwarzschild coordinates O($r, \vartheta, \varphi, ct$). The character of the constants in the OSM can also be better discerned in the former frame.

We derived the formula giving the acceleration of a TP in the vicinity of an MP when both particles are in rest. According to our result, the relativistic acceleration consists of two terms implying partial accelerations in mutually opposite directions. The first term is related to the attractive gravity and it is identical with the gravitational acceleration derived from the Newton gravitational law. The second term, the size of which is smaller than the size of the first one above the event horizon (except for some special distributions of matter), implies a certain reduction of the acceleration in a simple case of the gravitational action between two objects. The second term can also be represented as the relativistic, repulsive, complement of the Newtonian formula.

# References

deLyra, J. L., Energetic Stability of the Solutions of the Einstein Field Equations for Spherically Symmetric Liquid Shells. 2021, *arXiv e-prints*, arXiv:2101.07214, DOI: 10.48550/arXiv.2101.07214

deLyra, J. L. & Carneiro, C. E. I., Complete solution of the Einstein field equations for a spherical distribution of polytropic matter. 2023, *General Relativity and Gravitation*, **55**, 67, DOI: 10.1007/s10714-023-03115-6

deLyra, J. L., de A. Orselli, R., & Carneiro, C. E. I., Exact solution of the Einstein field equations for a spherical shell of fluid matter. 2023, *General Relativity and Gravitation*, **55**, 68, DOI: 10.1007/s10714-023-03116-5

Einstein, A., Die Feldgleichungen der Gravitation. 1915, *Sitzungsberichte der K&ouml;niglich Preussischen Akademie der Wissenschaften*, 844

Einstein, A., Die Grundlage der allgemeinen Relativitätstheorie. 1916, *Annalen der Physik*, **354**, 769, DOI: 10.1002/andp.19163540702

Neslušan, L., The Ni's Solution for Neutron Star and Outward Oriented Gravitational Attraction in Its Interior. 2015, *Journal of Modern Physics*, **6**, 2164, DOI: 10.4236/jmp.2015.615220

Neslušan, L., A solution to unconstrained Einstein's equations for a relativistic radiation sphere. in , *New Frontiers in Black Hole Astrophysics*, ed. A. Gomboc, Vol. **324**, 355–356

Neslušan, L., Outline of the concept of stable relativistic radiation sphere. A model of quasar? 2017b, *Astrophysics and Space Science*, **362**, 48, DOI: 10.1007/s10509-017-3027-x

Neslušan, L., The second rise of general relativity in astrophysics. 2019, *Modern Physics Letters A*, **34**, 1950244, DOI: 10.1142/S0217732319502444

Neslušan, L., A demonstration of the difference between the normalized and normalized and non-limited solutions of the field equations in the modeling of relativistic compact objects. 2022, in *Cosmology on Small Scales 2022. Dark Energy and the Local Hubble Expansion Problem*, ed. M. Křížek & Y. V. Dumin (Institute of Mathematics, Czech Academy of Sciences), 85–102

Ni, J., Solutions without a maximum mass limit of the general relativistic field equations for neutron stars. 2011, *Science China Physics, Mechanics, and Astronomy*, **54**, 1304, DOI: 10.1007/s11433-011-4350-9

Schwarzschild, K., Über das Gravitationsfeld einer Kugel aus inkompressibler Flüssigkeit nach der Einsteinschen Theorie. 1916, in *Sitzungsberichte der Königlich Preussischen Akademie der Wissenschaften zu Berlin*, 424–434

Straumann, N. 2013, *General Relativity* (Springer)

# A. Metric tensor in O($x,y,z,\tau$) frame

Using the general transformation formula (27), the components of the metric tensor, $g_{\alpha\beta}$, in the O($x,y,z,\tau$) coordinate frame can be calculated and the result is:

$$g_{11} \equiv g_{xx} = \frac{x^2}{R^2}g_{rr} - \frac{x^2 z^2}{R^2 \rho^2} - \frac{y^2}{\rho^2}, \tag{A1}$$

$$g_{12} \equiv g_{xy} = \frac{xy}{R^2}g_{rr} - \frac{xy z^2}{R^2 \rho^2} + \frac{xy}{\rho^2}, \tag{A2}$$

$$g_{13} \equiv g_{xz} = \frac{xz}{R^2}g_{rr} + \frac{xz}{R^2}, \tag{A3}$$

$$g_{14} \equiv g_{x\tau} = 0, \tag{A4}$$

$$g_{22} \equiv g_{yy} = \frac{y^2}{R^2}g_{rr} - \frac{y^2 z^2}{R^2 \rho^2} - \frac{x^2}{\rho^2}, \tag{A5}$$

$$g_{23} \equiv g_{yz} = \frac{yz}{R^2}g_{rr} + \frac{yz}{R^2}, \tag{A6}$$

$$g_{24} \equiv g_{y\tau} = 0, \tag{A7}$$

$$g_{33} \equiv g_{zz} = \frac{z^2}{R^2}g_{rr} - \frac{\rho^2}{R^2}, \tag{A8}$$

$$g_{34} \equiv g_{z\tau} = 0, \tag{A9}$$

$$g_{44} \equiv g_{\tau\tau} = g_{tt}. \tag{A10}$$

Since the product of two derivatives is commutative, i.e. $(\partial x^\alpha / \partial x^\mu)(\partial x^\beta / \partial x^\nu) = (\partial x^\beta / \partial x^\nu)(\partial x^\alpha / \partial x^\mu)$, and $g_{\mu\nu} = g_{\nu\mu}$ in the Schwarzschild coordinates, it is also valid that

$$g_{\alpha\beta} = g_{\beta\alpha}. \tag{A11}$$

In other words, the tensor $g_{\alpha\beta}$ in the O($x,y,z,\tau$) coordinate system can be given as

$$g_{\alpha\beta} = \begin{pmatrix} g_{xx} & g_{xy} & g_{xz} & 0 \\ g_{xy} & g_{yy} & g_{yz} & 0 \\ g_{xz} & g_{yz} & g_{zz} & 0 \\ 0 & 0 & 0 & g_{\tau\tau} \end{pmatrix} \tag{A12}$$

If the TP is located on the coordinate $x$-axis, then $y = z = 0$ and the the spatial components of the metric tensor $g_{\alpha\beta}$ reduce to

$$g_{xx} = g_{rr}, \tag{A13}$$

$$g_{yy} = -1, \tag{A14}$$

$$g_{zz} = -1, \tag{A15}$$

$$g_{\alpha\beta} = 0 \qquad \text{for} \;\; \alpha \neq \beta. \tag{A16}$$

# B. Contravariant components of metric tensor

To calculate the Christoffel symbols (in Appendix C), we need to know the contravariant form of the metric tensor $g_{\alpha\beta}$. It is well known that the covariant and contravariant components are related by the formula

$$g_{\alpha\sigma}g^{\sigma\beta} = \delta_\alpha^\beta, \tag{B1}$$

where $\delta_\alpha^\beta$ is the Kronecker delta (it is equal to 1 if $\alpha = \beta$ and 0 if $\alpha \neq \beta$).

When we use relation (B1), the fact that $g_{\alpha\beta} = g_{\beta\alpha}$, and omit zero terms, we can write the following five sets of equations:

1-st set:

$$g_{11}g^{11} + g_{12}g^{21} + g_{13}g^{31} = 1, \tag{B2}$$
$$g_{12}g^{11} + g_{22}g^{21} + g_{23}g^{31} = 0, \tag{B3}$$
$$g_{13}g^{11} + g_{23}g^{21} + g_{33}g^{31} = 0, \tag{B4}$$
$$\tag{B5}$$

2-nd set:

$$g_{11}g^{12} + g_{12}g^{22} + g_{13}g^{32} = 0, \tag{B6}$$
$$g_{12}g^{12} + g_{22}g^{22} + g_{23}g^{32} = 1, \tag{B7}$$
$$g_{13}g^{12} + g_{23}g^{22} + g_{33}g^{32} = 0, \tag{B8}$$
$$\tag{B9}$$

3-rd set:

$$g_{11}g^{13} + g_{12}g^{23} + g_{13}g^{33} = 0, \tag{B10}$$
$$g_{12}g^{13} + g_{22}g^{23} + g_{23}g^{33} = 0, \tag{B11}$$
$$g_{13}g^{13} + g_{23}g^{23} + g_{33}g^{33} = 1, \tag{B12}$$
$$\tag{B13}$$

4-th set:

$$g_{11}g^{14} + g_{12}g^{24} + g_{13}g^{34} = 0, \tag{B14}$$
$$g_{12}g^{14} + g_{22}g^{24} + g_{23}g^{34} = 0, \tag{B15}$$
$$g_{13}g^{14} + g_{23}g^{24} + g_{33}g^{34} = 0, \tag{B16}$$
$$\tag{B17}$$

5-th set:

$$g_{44}g^{41} = 0, \tag{B18}$$
$$g_{44}g^{42} = 0, \tag{B19}$$
$$g_{44}g^{43} = 0, \tag{B20}$$
$$g_{44}g^{44} = 1. \tag{B21}$$

Since $g_{44} \neq 0$, Set 5 immediately implies $g^{41} = g^{42} = g^{43} = 0$ and $g^{44} = 1/g_{44}$. Each of Sets 1 to 4 is the system of three equations with three unknown variables. We can use the method of determinants to solve each system. The basic determinant is the same for all four sets,

$$D = \begin{vmatrix} g_{11} & g_{12} & g_{13} \\ g_{12} & g_{22} & g_{23} \\ g_{13} & g_{23} & g_{33} \end{vmatrix} \equiv \begin{vmatrix} g_{xx} & g_{xy} & g_{xz} \\ g_{xy} & g_{yy} & g_{yz} \\ g_{xz} & g_{yz} & g_{zz} \end{vmatrix} =$$

$$= g_{xx}g_{yy}g_{zz} + 2g_{xy}g_{xz}g_{yz} - g_{xz}^2 g_{yy} - g_{xy}^2 g_{zz} - g_{xx}g_{yz}^2. \tag{B22}$$

After we solve the system of equations, we obtain:
from Set 1:

$$g^{11} \equiv g^{xx} = \frac{1}{D}(g_{yy}g_{zz} - g_{yz}^2), \tag{B23}$$

$$g^{21} \equiv g^{yx} = \frac{1}{D}(g_{xz}g_{yz} - g_{xy}g_{zz}), \tag{B24}$$

$$g^{31} \equiv g^{zx} = \frac{1}{D}(g_{xy}g_{yz} - g_{xz}g_{yy}); \tag{B25}$$

from Set 2:

$$g^{12} \equiv g^{xy} = \frac{1}{D}(g_{xz}g_{yz} - g_{xy}g_{zz}), \tag{B26}$$

$$g^{22} \equiv g^{yy} = \frac{1}{D}(g_{xx}g_{zz} - g_{xz}^2), \tag{B27}$$

$$g^{32} \equiv g^{zy} = \frac{1}{D}(g_{xy}g_{xz} - g_{xx}g_{yz}); \tag{B28}$$

from Set 3:

$$g^{13} \equiv g^{xz} = \frac{1}{D}(g_{xy}g_{yz} - g_{xz}g_{yy}), \tag{B29}$$

$$g^{23} \equiv g^{yz} = \frac{1}{D}(g_{xy}g_{xz} - g_{xx}g_{yz}), \tag{B30}$$

$$g^{33} \equiv g^{zz} = \frac{1}{D}(g_{xx}g_{yy} - g_{xy}^2); \tag{B31}$$

and from Set 4: $g^{14} \equiv g^{x\tau} = 0$, $g^{24} \equiv g^{y\tau} = 0$, and $g^{34} \equiv g^{z\tau} = 0$. We see that $g^{\alpha 4} = g^{4\alpha}$.

Let us now derive the determinant $D$ and the contravariant components explicitly. The determinant, given by relation (B22), can be re-written as

$$D = g_{xx}A + g_{xz}B + g_{xy}C, \tag{B32}$$

where we denoted

$$A = g_{xx}g_{zz} - g_{yz}^2, \tag{B33}$$

$$B = g_{xy}g_{yz} - g_{xz}g_{yy}, \tag{B34}$$

$$C = g_{xz}g_{yz} - g_{xy}g_{zz}. \tag{B35}$$

When we supply the explicit forms of the $g_{\alpha\beta}$ components given by relations (A1) to (A8) into the last three relations, we obtain

$$A = \frac{1}{R^2} \left[ x^2 - \left( y^2 + z^2 \right) g_{rr} \right],$$ (B36)

$$B = \frac{xz}{R^2} \left( g_{rr} + 1 \right),$$ (B37)

$$C = \frac{xy}{R^2} \left( g_{rr} + 1 \right),$$ (B38)

and the determinant

$$D = g_{rr}$$ (B39)

after some algebraic handling.

When relations (A1) to (A8) and (B39) are supplied into (B23), (B26), and (B29), they acquire the form

$$g^{xx} = \frac{x^2}{R^2} \left( 1 + \frac{1}{g_{rr}} \right) - 1,$$ (B40)

$$g^{xy} = \frac{xy}{R^2} \left( 1 + \frac{1}{g_{rr}} \right),$$ (B41)

$$g^{xz} = \frac{xz}{R^2} \left( 1 + \frac{1}{g_{rr}} \right).$$ (B42)

For a particle situated on the coordinate $x$-axis, we can prove that the only non-zero contravariant components are

$$g^{11} \equiv g^{xx} = \frac{1}{g_{xx}} = \frac{1}{g_{rr}},$$ (B43)

$$g^{22} \equiv g^{yy} = \frac{1}{g_{yy}} = -1,$$ (B44)

$$g^{33} \equiv g^{zz} = \frac{1}{g_{zz}} = -1,$$ (B45)

$$g^{44} \equiv g^{\tau\tau} = \frac{1}{g_{\tau\tau}}.$$ (B46)

## C. Christoffel symbols $\Gamma^1_{\beta\gamma}$ and $\Gamma^4_{\beta\gamma}$

We recall the well-known general formula to calculate the Christoffel symbols,

$$\Gamma^\alpha_{\beta\gamma} = \frac{1}{2} g^{\alpha\sigma} \left( \frac{\partial g_{\sigma\beta}}{\partial x^\gamma} + \frac{\partial g_{\sigma\gamma}}{\partial x^\beta} - \frac{\partial g_{\beta\gamma}}{\partial x^\sigma} \right). \tag{C1}$$

In the following, this formula is used to calculate the symbols figuring in relation (34) that we use in our derivation. At first, we give the implicit result.

The symbols with the upper index "1" are

$$\Gamma^1_{11} = \frac{1}{2} g^{11} \frac{\partial g_{11}}{\partial x^1} + g^{12} \frac{\partial g_{12}}{\partial x^1} - \frac{1}{2} g^{12} \frac{\partial g_{11}}{\partial x^2} + g^{13} \frac{g_{13}}{\partial x^1} - \frac{1}{2} g^{13} \frac{\partial g_{11}}{\partial x^3}, \tag{C2}$$

$$\Gamma^1_{12} = \frac{1}{2} g^{11} \frac{\partial g_{11}}{\partial x^2} + \frac{1}{2} g^{12} \frac{\partial g_{22}}{\partial x^1} + \frac{1}{2} g^{13} \left( \frac{\partial g_{13}}{\partial x^2} + \frac{\partial g_{23}}{\partial x^1} - \frac{\partial g_{12}}{\partial x^3} \right), \tag{C3}$$

$$\Gamma^1_{13} = \frac{1}{2} g^{11} \frac{\partial g_{11}}{\partial x^3} + \frac{1}{2} g^{12} \left( \frac{\partial g_{12}}{\partial x^3} + \frac{\partial g_{23}}{\partial x^1} - \frac{\partial g_{13}}{\partial x^3} \right) + \frac{1}{2} g^{13} \frac{\partial g_{33}}{\partial x^1}, \tag{C4}$$

$$\Gamma^1_{14} = 0, \tag{C5}$$

$$\Gamma^1_{21} = \frac{1}{2} g^{11} \frac{\partial g_{11}}{\partial x^2} + \frac{1}{2} g^{12} \frac{\partial g_{22}}{\partial x^1} + \frac{1}{2} g^{13} \left( \frac{\partial g_{23}}{\partial x^1} + \frac{\partial g_{13}}{\partial x^2} - \frac{\partial g_{12}}{\partial x^3} \right), \tag{C6}$$

$$\Gamma^1_{22} = g^{11} \frac{\partial g_{12}}{\partial x^2} - \frac{1}{2} g^{11} \frac{\partial g_{22}}{\partial x^1} + \frac{1}{2} g^{12} \frac{\partial g_{22}}{\partial x^2} + g^{13} \frac{\partial g_{23}}{\partial x^2} - \frac{1}{2} g^{13} \frac{\partial g_{22}}{\partial x^3}, \tag{C7}$$

$$\Gamma^1_{23} = \frac{1}{2} g^{11} \left( \frac{\partial g_{12}}{\partial x^3} + \frac{\partial g_{13}}{\partial x^2} - \frac{\partial g_{23}}{\partial x^1} \right) + \frac{1}{2} g^{12} \frac{\partial g_{22}}{\partial x^3} + \frac{1}{2} g^{13} \frac{\partial g_{33}}{\partial x^2}, \tag{C8}$$

$$\Gamma^1_{24} = 0, \tag{C9}$$

$$\Gamma^1_{31} = \frac{1}{2} g^{11} \frac{\partial g_{11}}{\partial x^3} + \frac{1}{2} g^{12} \left( \frac{\partial g_{23}}{\partial x^1} + \frac{\partial g_{12}}{\partial x^3} - \frac{\partial g_{13}}{\partial x^2} \right) + \frac{1}{2} g^{13} \frac{\partial g_{33}}{\partial x^1}, \tag{C10}$$

$$\Gamma^1_{32} = \frac{1}{2} g^{11} \left( \frac{\partial g_{13}}{\partial x^2} + \frac{\partial g_{12}}{\partial x^3} - \frac{\partial g_{23}}{\partial x^1} \right) + \frac{1}{2} g^{12} \frac{\partial g_{22}}{\partial x^3} + \frac{1}{2} g^{13} \frac{\partial g_{33}}{\partial x^2}, \tag{C11}$$

$$\Gamma^1_{33} = g^{11} \frac{\partial g_{13}}{\partial x^3} - \frac{1}{2} g^{11} \frac{\partial g_{33}}{\partial x^1} + g^{12} \frac{\partial g_{23}}{\partial x^3} - \frac{1}{2} g^{12} \frac{\partial g_{33}}{\partial x^2} + \frac{1}{2} g^{13} \frac{\partial g_{33}}{\partial x^3}, \tag{C12}$$

$$\Gamma^1_{34} = 0, \tag{C13}$$

$$\Gamma^1_{41} = 0, \tag{C14}$$

$$\Gamma^1_{42} = 0, \tag{C15}$$

$$\Gamma^1_{43} = 0, \tag{C16}$$

$$\Gamma^1_{44} = -\frac{1}{2} g^{11} \frac{\partial g_{44}}{\partial x^1} - \frac{1}{2} g^{12} \frac{\partial g_{44}}{\partial x^2} - \frac{1}{2} g^{13} \frac{\partial g_{44}}{\partial x^3}. \tag{C17}$$

Notice that $\Gamma^1_{\alpha\beta} = \Gamma^1_{\beta\alpha}$.

The non-zero symbols with the upper index "4" are

$$\Gamma^4_{14} = \Gamma^4_{41} = \frac{1}{2} g^{44} \frac{\partial g_{44}}{\partial x^1}, \tag{C18}$$

$$\Gamma^4_{24} = \Gamma^4_{42} = \frac{1}{2} g^{44} \frac{\partial g_{44}}{\partial x^2}, \tag{C19}$$

$$\Gamma^4_{34} = \Gamma^4_{43} = \frac{1}{2} g^{44} \frac{\partial g_{44}}{\partial x^3}. \tag{C20}$$

When the TP and MP are in rest, we need to know, explicitly, only symbol $\Gamma^1_{44} \equiv \Gamma^x_{\tau\tau}$ to calculate the $x$-component of the acceleration. In the simplest case, when the TP is situated on the coordinate $x$-axis, i.e. $y = z = 0$, we found, in Appendix B, that $g^{xy} = g^{xz} = 0$. Using these expressions and relation (B43), relation (C17) reduces to

$$\Gamma^1_{44} \equiv \Gamma^x_{\tau\tau} = -\frac{1}{2g_{xx}}\frac{\partial g_{\tau\tau}}{\partial x}. \tag{C21}$$

# Photospheric aluminium abundances of A-type main-sequence stars

**Y. Takeda**[ID]

*11-2 Enomachi, Naka-ku, Hiroshima-shi, 730-0851, Japan (E-mail:
ytakeda@js2.so-net.ne.jp)*

**Abstract.** Although anomalous surface abundances are often observed in A-type main-sequence stars (known as chemically peculiar stars; e.g., metallic line stars or Am stars), our understanding about the behavior of aluminium is still insufficient. Actually, even whether Al is overabundant or underabundant in Am stars is not clarified. This is presumably because most of the previous studies employed the Al I 3944/3961 lines with the assumption of LTE, despite that a considerable non-LTE effect is expected in this resonance doublet. With an aim to shed light on this issue, extensive statistical-equilibrium calculations on Al I/Al II were carried out for a wide range of atmospheric parameters, based on which the non-LTE Al abundances were determined by applying the spectrum-fitting technique to the Al I 3944/3961 lines for 63 A-type dwarfs ($7000 \lesssim T_{\mathrm{eff}} \lesssim 10000$ K) of comparatively lower rotational velocities ($v_{\mathrm{e}} \sin i \lesssim 100$ km s$^{-1}$). The following results were obtained. (1) The non-LTE corrections ($\Delta$) are positive (reflecting the importance of overionization) and significantly large ($0.3 \lesssim \Delta \lesssim 1.0$ dex depending on $T_{\mathrm{eff}}$; generally $\Delta_{3944} < \Delta_{3961}$). (2) By applying these corrections (and indispensable inclusion of Balmer line wings as background opacity), consistent non-LTE abundances for both lines could be obtained, and the serious zero-point discrepancy (considerably negative [Al/H] for normal metallicity stars of [Fe/H] $\sim 0$) found in old studies has been settled. (3) Al abundances of A-type stars are almost in proportion to [Fe/H] (tending to be overabundant in Am stars) with an approximate relation of [Al/H] $\sim$ 1.2 [Fe/H], which is qualitatively consistent with the prediction of the diffusion theory (suggesting an Al excess in the photosphere of Am stars).

**Key words:** physical processes: diffusion – stars: abundances – stars: atmospheres – stars: chemically peculiar – stars: early-type

## 1. Introduction

An appreciable fraction of A-type stars ($7000 \lesssim T_{\mathrm{eff}} \lesssim 10000$ K) on the upper main sequence are chemical peculiar (CP) stars. Among these, A-type metallic-line (Am) stars are commonly observed in comparatively slower rotators ($v_{\mathrm{e}} \sin i \lesssim 100$ km $^{-1}$). While it is known that they show contrasting surface abundance anomalies between lighter and heavier elements (e.g., deficiency in

C, N, O, Ca, Sc; overabundances in Fe-group or s-process ones), abundance behaviors of those with intermediate atomic number ($10 < Z < 20$) are not necessarily well understood.

One of such elements for which abundances are poorly determined is aluminium (Al, $Z = 13$). This is not due to the lack of available lines, as strong resonance doublet lines of neutral aluminium at 3944 and 3961 Å are observable in the spectra of most A-type stars, although most Al atoms are in the once-ionized stage and only a tiny fraction remains neutral in stellar atmospheres of this $T_{\mathrm{eff}}$ range (Fig. 1). Actually, determinations of Al abundances in normal A-type and Am stars by using Al I 3944/3961 were reported already in the early work about a half century ago (e.g., Conti 1970; Smith 1971, 1973).
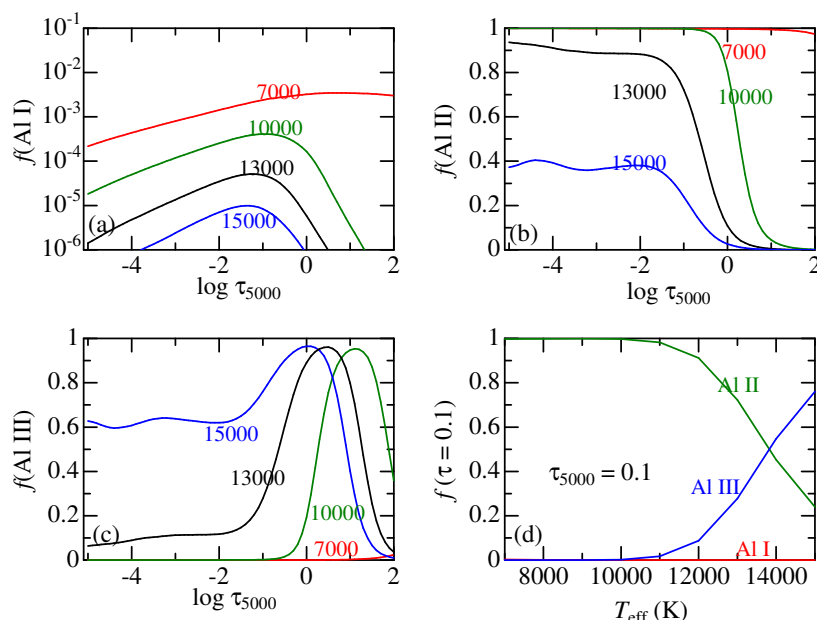


**Figure 1.** Number population fraction ($f$) of (a) neutral, (b) once-ionized, and (c) twice-ionized aluminium species relative to the total Al atoms [e.g., $f(\mathrm{Al\ I})$ $\equiv N(\mathrm{Al\ I})/N_{\mathrm{total}}^{\mathrm{Al}}$], plotted against the continuum optical depth at 5000 Å. Calculations were done for four $\log g = 4.0$ models of different $T_{\mathrm{eff}}$ (7000, 10000, 13000, and 15000 K) as indicated in each panel. The runs of $f$ for these three stages at $\tau_{5000} = 0.1$ with $T_{\mathrm{eff}}$ are also depicted in panel (d). All these calculations were done in LTE (use of Saha's equation).

Nevertheless, what was argued in those old studies was only qualitative that Al abundances in Am stars are comparatively higher than those in normal stars, while nothing could be said about the quantitative extent of Al anomalies with
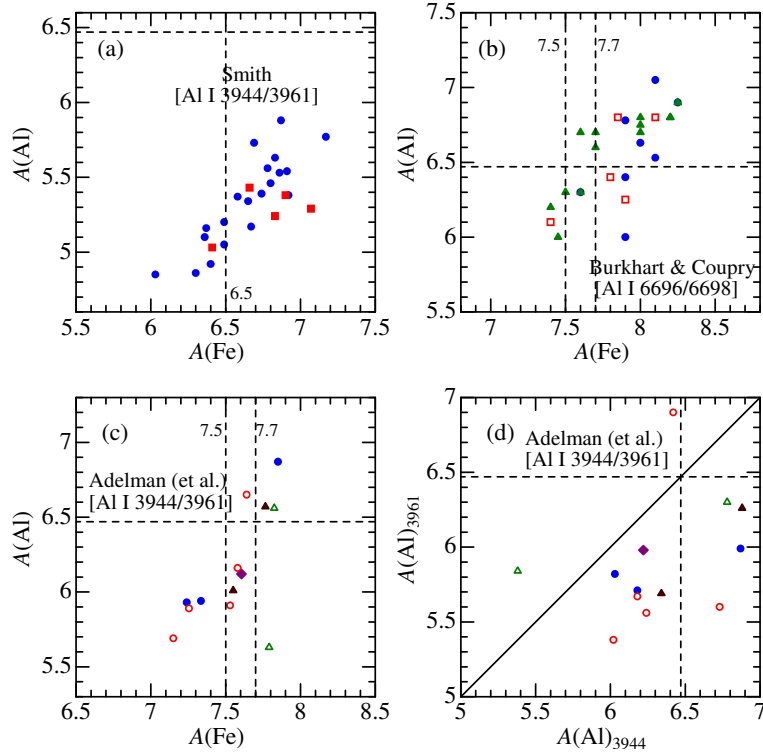
**Figure 2.** Panels (a)–(c) show the correlations of Al and Fe abundances published in the past literature. (a) Data of Smith (1971; circles) and Smith (1973; squares) based on Al I 3944/3961 lines. (b) Data of Burkhart and Coupry (1989–circles; 1991–triangles, 2000–squares) based on Al I 6696/6698 lines. (c) Data of Adelman (1984–filled diamond), Adelman et al. (1984–open triangles), Adelman (1988–filled triangles), Adelman (1994–filled circles), and Adelman et al. (1997–open circles) based on Al I 3944/3961 lines. (d) $A_{3944}$ vs. $A_{3961}$ relation for Adelman et al.'s data in panel (c). In each panel, the locations of the solar Al abundance of $A_{\odot}(\mathrm{Al}) = 6.47$ (adopted in this study) as well as of the solar Fe abundances believed at the time of the relevant papers (considerably revised over the past half century; cf. footnote 1) are indicated by dashed lines.

respect to the reference normal (solar) abundance[1] because absolute values of

---

[1] The solar photospheric abundance of aluminium $A_{\odot}(\mathrm{Al})$ is considered to be well established ($A$ is the logarithmic number abundance of the element relative to that of hydrogen with the usual normalization of $A = 12.00$ for H), for which quite similar values have been reported so far: 6.40 (Lambert, Warner 1968), 6.47 (Anders, Grevesse 1989), 6.45 (Asplund et al. 2009) In this paper, Anders and Grevesse's $A_{\odot}(\mathrm{Al})$ of 6.47 is adopted, as done in Kurucz's (1993) ATLAS9/WIDTH9 program. In contrast, $A_{\odot}(\mathrm{Fe})$ has experienced considerable updates from low-scale to high-scale over the past half century, mainly due to the large revision in the

the resulting Al abundances were far from reliable.

Since surface abundances of normal A-type stars of population I without chemical peculiarities should be more or less similar to the solar composition, $[\mathrm{Al/H}] \sim 0$ is expected to hold for stars of $[\mathrm{Fe/H}] \sim 0$.[2] However, according to Fig. 2a, where the Al abundances of A and Am stars derived by Smith (1971, 1973) from Al I 3944/3961 are plotted against the corresponding Fe abundances, the intercept of $[\mathrm{Al/H}]$ at $[\mathrm{Fe/H}] \sim 0$ is considerably subsolar ($\lesssim -1$ dex), which suggests that his $A(\mathrm{Al})$ values were significantly underestimated. This zero-point discrepancy ($[\mathrm{Al/H}] < 0$ at $[\mathrm{Fe/H}] \sim 0$) is similarly observed in Adelman et al.'s results (cf. Fig. 2c), who also employed the Al I 3944/3961 lines for deriving the Al abundances of A-type stars. To make things more complicated, the abundances they derived from these two lines are systematically discordant from each other ($A_{3961} < A_{3944}$; cf. Fig. 2d). These are the problems involved with Al abundance determinations using these resonance lines.

Admittedly, this problem may be circumvented by invoking other Al lines. As a matter of fact, Burkhart and Coupry (1989, 1991, 2000) employed the high-excitation Al I 6696/6698 lines to derive Al abundances for late A-type and Am/Fm stars in the field and open clusters, and the resulting $[\mathrm{Al/H}]$ values appear to favorably satisfy the requirement ($[\mathrm{Al/H}] \sim 0$ at $[\mathrm{Fe/H}] \sim 0$) mentioned above (cf. Fig. 2b). Unfortunately, these lines are so weak that are usable only for sharp-lined lower $T_{\mathrm{eff}}$ ($\lesssim 8000$ K) stars, which makes their applicability seriously limited. Accordingly, there is no other way than to avail of the strong Al I lines in the violet region if Al abundance behaviors of A-type stars in general are to be investigated.

Then, why are the Al abundances determined from 3944/3961 lines in the old studies unreliable and subject to appreciable errors (i.e., significantly underestimated)? The most likely reason is that they adopted the assumption of LTE in their analysis, because these Al I resonance lines are known to suffer a considerable non-LTE effect mainly caused by the overionization mechanism. Actually, Steenbock and Holweger (1992) carried out a statistical-equilibrium calculation in their analysis of Al I 3944 and 3961 lines of Vega and showed that rather large (positive) non-LTE corrections ($+0.4$ and $+0.7$ dex, respectively) should be applied. Since this correction acts in the direction of mitigating the underestimation, the problems involved in the Al abundances determined from 3944/3961 lines may be resolved by correctly taking into account the non-LTE effect.

However, ever since Steenbock and Holweger's (1992) non-LTE work confined to the specific case of Vega (a mildly metal-deficient A0V star), any investigation on the non-LTE effect of Al lines with regard to A-type stars in general has not been carried out to the author's knowledge, despite that not a few

---

transition probabilities of Fe lines (e.g., 6.5–7.0 → 7.3–7.7 → ∼ 7.5; see Fig. 1 in Grevesse, Sauval 1999), though it is eventually settled around 7.50 at present (cf. Asplund et al. 2009).

[2] As usual, $[\mathrm{X/H}]$ is the differential abundance of element X relative to the Sun; i.e., $[\mathrm{X/H}] \equiv A_{\mathrm{star}}(\mathrm{X}) - A_{\odot}(\mathrm{X})$.

non-LTE studies on Al I line formation for late-type stars (FGK type stars of $T_{\rm eff} \lesssim 6500$ K; especially in the metal-poor regime for studying galactic chemical evolution) have already been published in the past quarter century (Baumüller, Gehren 1996, 1997; Mashonkina et al. 2008; Andrievsky et al. 2008; Nordlander, Lind 2017; Ezzeddine et al. 2018).

Motivated by this situation, the author decided to conduct extensive non-LTE calculations on Al I+Al II for a wide range of atmospheric parameters (covering main-sequence stars of mid-F through late-B types), and apply them to the analysis of Al I 3944/3961 lines for a sufficient number of A-type dwarfs by making use of the available high-dispersion spectra. The points intended to clarify in this investigation are as follows.

– How are the behaviors (e.g., characteristic trends, dependence upon atmospheric parameters) of the non-LTE effect for Al I 3944 and 3961 resonance doublet lines in upper main-sequence stars? Is there any significant difference between these two lines?

– To establish the Al abundance trends of A-type stars (Am and normal A stars) of various [Fe/H] by applying the spectrum-fitting analysis to the 3944/3961 lines. Can the zero-point problem of [Al/H] seen in the old LTE work be removed by including the non-LTE corrections? Are the non-LTE abundances derived from 3944 and 3961 lines consistent with each other?

– Possibilities of Al abundance determination based on the other lines (than the Al I resonance lines of primary concern) are also examined, such as Al I 6696/6698 lines (used by Burkhart and Coupry) or Al II 3900/4663 lines (which have barely been employed in A-type stars). How are the non-LTE corrections for these lines?

## 2. Non-LTE calculation for Al

### 2.1. Atomic model and computational details

The statistical-equilibrium calculations for aluminium were carried out by using the non-LTE code described in Takeda (1991). The atomic model of Al adopted in this study was constructed based on Kurucz and Bell's (1995) compilation of atomic data ($gf$ values, levels, etc.), which consists of 65 Al I terms (up to $26s\ {}^2{\rm S}$ at 48092 cm$^{-1}$) with 218 Al I radiative transitions, 68 Al II terms (up to $10p\ {}^3{\rm P^o}$ at 146602 cm$^{-1}$) with 601 Al II radiative transitions, and 32 Al III terms (up to $9h\ {}^2{\rm H^o}$ at 217252 cm$^{-1}$; included only for conservation of total Al atoms). The ground ${}^2{\rm P^o}$ term of Al I (comprising two closely lying levels with statistical weights of $g = 2$ and 4 correspondig to $J = 1/2$ and $3/2$) was treated as a single level with $g = 6$.

Regarding the calculation of photoionization rates, the cross-section data taken from the TOPbase (Cunto, Mendoza 1992) were used for the lower 10

Al I terms and 10 Al II terms (while hydrogenic approximation was assumed for all other higher terms). As to the collisional (excitation and ionization) rates due to electron as well as neutral hydrogen, the recipe described in Sect. 3.1.3 of Takeda (1991) was followed. Inelastic collisions due to neutral hydrogen atoms were formally included by the analytical formula as described therein with a moderate scaling factor of $S_H = 0.4$ by following Steenbock and Holweger (1992) as well as Baumüller and Gehren (1997), though the effect of neutral hydrogen collision is insignificant in the atmosphere of early-type stars ($T_{eff} \gtrsim 7000$ K) under question.

The calculations were done on a grid of 192 ($= 12 \times 4 \times 4$) Kurucz's (1993) ATLAS9 models atmospheres (scaled solar-abundance models according to the metallicity [Fe/H]) resulting from combinations of twelve $T_{eff}$ values (6500, 7000, 7500, 8000, 8500, 9000, 9500, 10000, 11000, 12000, 13000, and 14000 K) and four $\log g$ values (3.0, 3.5, 4.0, and 4.5), and four [Fe/H] values ($-1.0$, $-0.5$, 0.0, and $+0.5$) while assuming $\xi = 2$ km s$^{-1}$ (microturbulence) and metallicity-scaled abundances of $A(Al) = 6.47 + [Fe/H]$ (where 6.47 is the solar Al abundance used in Kurucz's ATLAS9 models) were adopted as the input Al abundance.

## 2.2. Behaviors of non-LTE departure coefficients

The non-LTE departure coefficients of the representative four Al terms calculated for the model corresponding to Vega are plotted against the optical depth in Fig. 3. Comparing this figure with Fig. 2 of Steenbock and Holweger (1992), we can see that both calculations are reasonably consistent with each other.
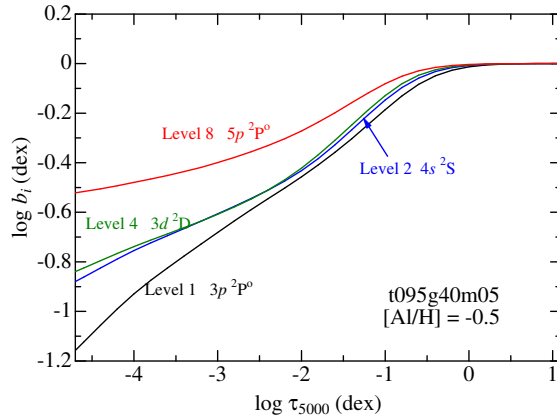


**Figure 3.** Run of the non-LTE departure coefficients ($b_i \equiv n_i^{NLTE}/n_i^{LTE}$) of neutral Al atom with the continuum optical depth at 5000 Å calculated for the model of $T_{eff} = 9500$ K, $\log g = 4.0$, and [M/H] = [Fe/H] = [Al/H] = $-0.5$. Shown here are the results for the selected lower 4 terms of $3p$ $^2$P$^o$, $4s$ $^2$S, $3d$ $^2$D, and $5p$ $^2$P$^o$ ($i = 1, 2, 4,$ and 8). This figure is arranged so as to be compared with Steenbock and Holweger's (1992) Fig. 2.
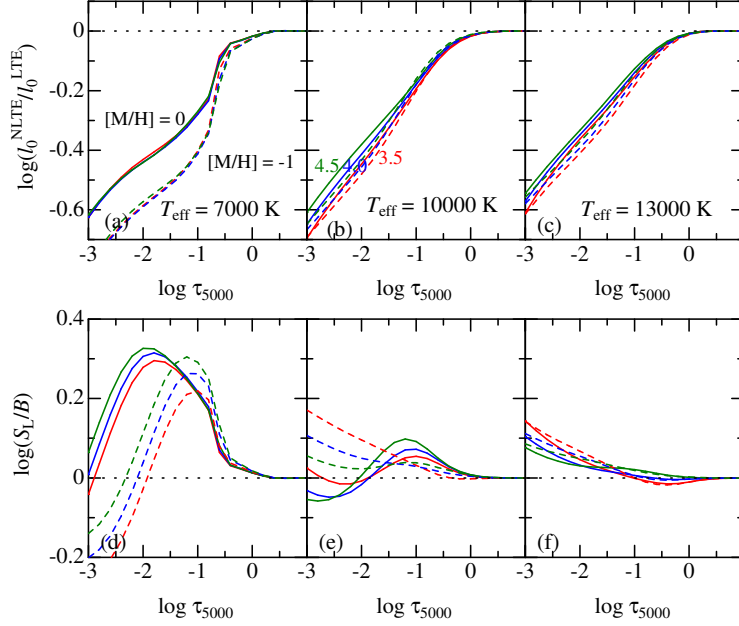
**Figure 4.** The non-LTE-to-LTE line-center opacity ratio (upper panels a–c) and the ratio of the line source function ($S_L$) to the local Planck function ($B$) (lower panels d–f) for the Al I $3p\ ^2P^o$–$4s\ ^2S$ transition (corresponding to Al I 3944/3961 lines) of multiplet 1, plotted against the continuum optical depth at 5000 Å. Shown here are the calculations done with $\xi = 2$ km s$^{-1}$ on the solar-metallicity models ([M/H] = [Fe/H] = 0; solid lines) and $1/10\times$ metal-deficient models ([M/H] = [Fe/H] = $-1$; dashed lines) of $T_{\mathrm{eff}}$ = 7000 K (left panels a, d), 10000 K (middle panels b, e), and 13000 K (right panels c, f), where metallicity-scaled Al abundance ([Al/Fe] = 0) was adopted in the calculation. At each panel, the results for three $\log g$ values of 3.5, 4.0, and 4.5 are depicted by different colors (red, blue, and green, respectively).

Fig. 4 also shows the $l_0^{\mathrm{NLTE}}(\tau)/l_0^{\mathrm{LTE}}(\tau)$ (the non-LTE-to-LTE line-center opacity ratio; almost equal to $\simeq b_1$) and $S_L(\tau)/B(\tau)$ (the ratio of the line source function to the Planck function; nearly equal to $\simeq b_2/b_1$) for the transition relevant to the Al I 3944/3961 lines ($b_1$ and $b_2$ are the non-LTE departure coefficients for the lower and upper terms), which were computed on the models of representative $T_{\mathrm{eff}}$ and $\log g$ values.

As seen from this figure, the inequality relation $l_0^{\mathrm{NLTE}}/l_0^{\mathrm{LTE}} < 1$ (underpopulation or overionization) prevails in all depths, and the relation $S_L/B \gtrsim 1$ (enhancement of the line source function) tends to hold in the line-forming region, both acting in the direction of weakening the strengths of absorption lines. Therefore, the Al I resonance doublet lines at 3944/3961 Å are weakened

by the non-LTE effect. Since this non-LTE underpopulation is due to the overi-
onization mechanism caused by the imbalance between the photoionization and
photorecombination rates ($J > B$), its extent may be sensitive to the metallic-
ity ([M/H]) which generally plays an important role for the UV radiation field.
According to Fig. 4, however, the effect of changing [M/H] is not so significant
except for the case of lower $T_{\rm eff}$ (7000 K).

**Table 1.** Adopted atomic data of Al lines.

| Species | Multiplet No. | $\lambda$ (Å) | $\chi_{\rm low}$ (eV) | $\log gf$ (dex) | Gammar (dex) | Gammas (dex) | Gammaw (dex) |
|---|---|---|---|---|---|---|---|
| Al I | 1 | 3944.006 | 0.000 | −0.623 | (8.16) | (−6.30) | −7.32 |
| Al I | 1 | 3961.520 | 0.014 | −0.323 | (8.16) | (−6.30) | −7.32 |
| Al I | 5 | 6696.023 | 3.143 | −1.347 | (7.70) | (−5.16) | (−7.28) |
| Al I | 5 | 6698.673 | 3.143 | −1.647 | (7.70) | (−5.16) | (−7.28) |
| Al II | 1 | 3900.675 | 7.421 | −1.270 | 9.22 | (−5.95) | (−7.77) |
| Al II | 2 | 4663.046 | 10.598 | −0.284 | 7.99 | (−5.53) | (−7.64) |

Note.
These data are were taken from the VALD database (Ryabchikova et al. 2015), while those
parenthesized are the default values calculated by Kurucz's (1993) WIDTH9 program.
Followed by first five self-explanatory columns, damping parameters are given in the last three
columns:
Gammar is the radiation damping width (s$^{-1}$), $\log \gamma_{\rm rad}$.
Gammas is the Stark damping width (s$^{-1}$) per electron density (cm$^{-3}$) at $10^4$ K, $\log(\gamma_{\rm e}/N_{\rm e})$.
Gammaw is the van der Waals damping width (s$^{-1}$) per hydrogen density (cm$^{-3}$) at $10^4$ K,
$\log(\gamma_{\rm w}/N_{\rm H})$.

## 2.3. Grid of abundance corrections

Based on the results of these calculations, theoretical equivalent-widths and the
corresponding non-LTE abundance corrections for Al I 3944 and 3961 lines were
computed for each of the models as follows. First, for an assigned Al abundance
($A = 6.47 +$ [Fe/H]) and microturbulence ($\xi$; any of 1, 2, 3, and 4 km s$^{-1}$),[3]
the non-LTE equivalent width ($W^{\rm N}$) of the line was calculated by using the
computed non-LTE departure coefficients ($b$) for each model atmosphere (LTE
equivalent width $W^{\rm L}$ was also calculated for comparison, though not used for
evaluation of $\Delta$). Next, the LTE ($A^{\rm L}$) and NLTE ($A^{\rm N}$) abundances were com-
puted from this $W^{\rm N}$ while regarding it as if being a given observed equivalent
width. We could then obtain the non-LTE abundance correction ($\Delta$), which is
defined in terms of these two abundances as $\Delta \equiv A^{\rm N} - A^{\rm L}$.

Here, Kurucz's (1993) WIDTH9 program, which was considerably modi-
fied in many respects (e.g., incorporation of non-LTE departure in the line
source function as well as in the line opacity, etc.), was employed for calcu-

---

[3]The departure coefficients computed for a fixed $\xi$ of 2 km s$^{-1}$ were applied also to the cases
of $\xi = 1$, 3, and 4 km s$^{-1}$ because they are not so sensitive to a choice of $\xi$.

lating the equivalent width for a given abundance, or inversely evaluating the abundance for an assigned equivalent width. The background opacities of overlapping Balmer lines, which are important for these Al lines in the violet region (especially for the 3961 line), were included as done in Kurucz's (1993) ATLAS9 program (Griem 1960, 1967). The adopted atomic data of these lines ($gf$ values, damping constants, etc.) are summarized in Table 1. The resulting grids of $W^{\mathrm{L}}$, $W^{\mathrm{N}}$, $A^{\mathrm{N}}$, $A^{\mathrm{L}}$, and $\Delta$ calculated for 3944 and 3961 lines are presented in the supplementary materials: 8 data files named as "`ncor####.%%%`", where '`####`' denotes the relevant line ('3944' or '3961') and '`%%%`' is the metallicity code ('m10', 'm05', 'p00', and 'p05' corresponding to [X/H] = [Fe/H] = $-1.0$, $-0.5$, 0.0, and +0.5, respectively).

### 2.4. Dependence of $W$ and $\Delta$ upon stellar parameters

How the theoretical $W$ and $\Delta$ computed for these two Al I lines depend upon the atmospheric parameters ($T_{\mathrm{eff}}$, $\log g$, and $\xi$) is illustrated in Fig. 5, from which the following characteristics are read.

–  The equivalent widths ($W$) progressively decrease with an increase in $T_{\mathrm{eff}}$, reflecting the $T$-dependence of $\propto \exp[\chi_{\mathrm{ion}}/(kT)]$ for the number population of the ground level ($k$ is the Boltzmann constant, $\chi_{\mathrm{ion}}$ is the ionization potential of 5.98 eV), while the inequality relation of $W^{\mathrm{N}} < W^{\mathrm{L}}$ (non-LTE line weakening) generally holds if compared at the same condition. Although the transition probability ($gf$ value) for the 3961 line is twice as stronger as that of the 3944 line (cf. Table 1), the difference between $W_{3944}$ and $W_{3961}$ is not so manifest, which is presumably because the latter $W_{3961}$ is more significantly affected by the opacity of H$\epsilon$ line wing (tending to weaken the line strength).

–  The non-LTE corrections are always positive ($\Delta > 0$) reflecting that the line is weakened by the non-LTE effect, and significantly large ($\sim 0.2$–1.0 dex). The $\Delta$ values appreciably depend upon $W$ (and thus upon $T_{\mathrm{eff}}$), tending to be larger with increasing $W$. This is because the line-forming region moves towards the upper layer (where the departure from LTE is more significant) until desaturation begins in the flat-to-damping transition part of the curve of growth ($W \gtrsim 200$ mÅ at $T_{\mathrm{eff}} \lesssim 8000$ K). Generally, $\Delta_{3944}$ is smaller than $\Delta_{3961}$, because the latter 3961 line (larger opacity) forms in a comparatively higher layer.

–  $W$ tends to decline with a decrease in $\log g$, because ionization is enhanced in the condition of lowered density. Since these lines are generally strong ($W \gtrsim 100$ mÅ) as to be in the flat part of the curve of growth, $W$ sensitively grows with an increase in $\xi$. The reason why $\Delta$ tends to increase with $\log g$ as well as $\xi$ can be understood in terms of the $W$-dependence of $\Delta$ mentioned above.
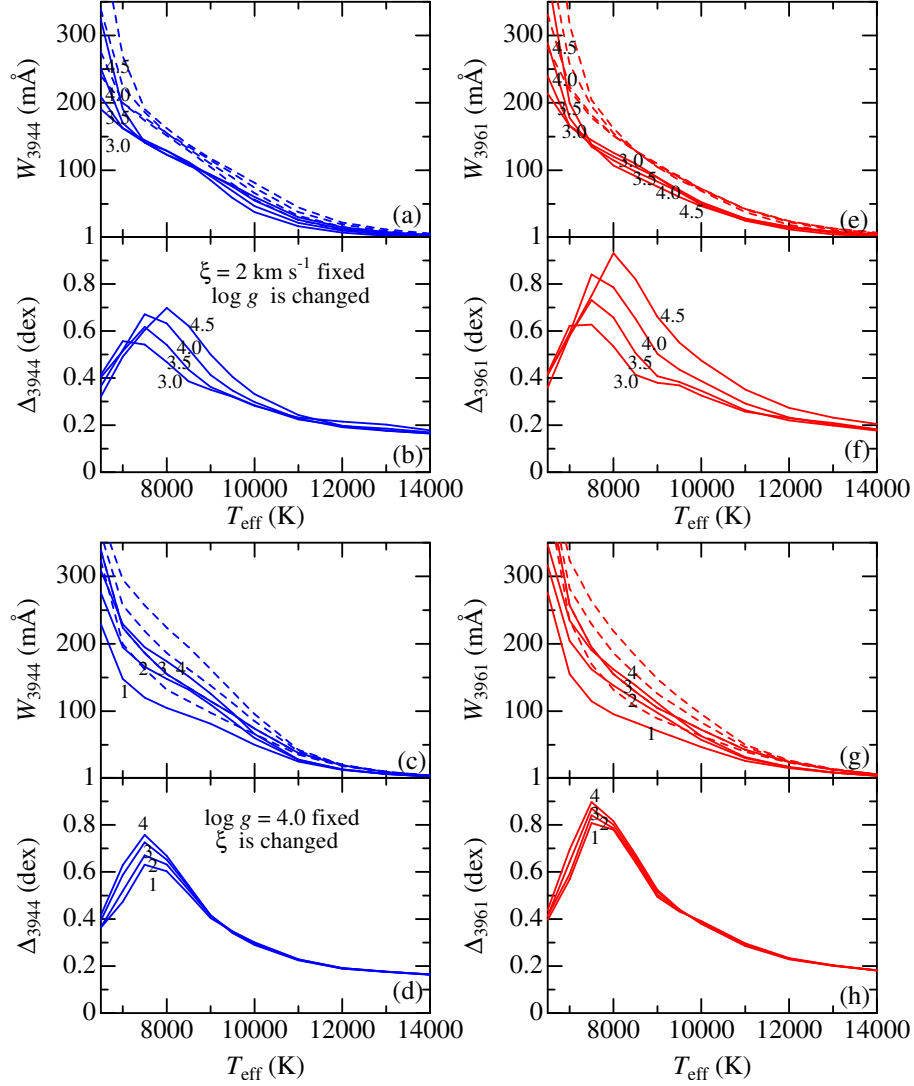
**Figure 5.** The non-LTE and LTE equivalent widths ($W^{\mathrm{N}}$ and $W^{\mathrm{L}}$) for the Al I 3944/3961 lines and the corresponding non-LTE corrections ($\Delta$), which were computed on the non-LTE grid of models described in Sect 2.1, are plotted against $T_{\mathrm{eff}}$. Each figure set consists of two panels; the upper panel is for $W^{\mathrm{N}}$ (solid lines) and $W^{\mathrm{L}}$ (dashed lines), while the lower panel is for $\Delta$. The upper sets (a+b, e+f) show the case of fixed $\xi$ (2 km s$^{-1}$) but different $\log g$ (3.0, 3.5, 4.0, and 4.5), while the lower sets (c+d, g+h) are for the case of fixed $\log g$ (4.0) but different $\xi$ (1, 2, 3, and 4 km s$^{-1}$). The left-hand figures show the results for the Al I 3944 line, while the right-hand ones for the Al I 3961 line.

## 3. Analysis of Al I 3944/3947 lines for A-type stars

### 3.1. Observational data

Our next task is to determine the Al abundances for a number of sample stars from the Al I resonance doublet lines at 3944 and 3961 Å by taking into account the non-LTE effect. Regarding the observational data for this purpose, Takeda et al.'s (2008, 2009) spectra of A-type stars obtained by BOES (Bohyunsan Observatory Echelle Spectrograph) were mainly used (Group B in Table 2), because they cover the relevant violet region thanks to their wide wavelength coverage, where stars are limited to those of low-to-moderate projected rotational velocities ($v_e \sin i \leq 100$ km s$^{-1}$) as done in Takeda et al. (2018) or Takeda (2022).

In addition, the spectra of 7 sharp-lined particularly bright A-type stars were secured by new observations specifically directed to the shorter wavelength region (Group A in Table 2), which were carried out on 2016 November 2–6 at the Okayama Astrophysical Observatory by using the 188 cm reflector along with HIDES (HIgh Dispersion Echelle Spectrograph) in the mode of a blue cross disperser. The data reduction was done in the standard manner by using IRAF,[4] by which the spectra covering 3300–5600 Å with a resolving power of $R \sim 100000$ were obtained. The finally resulting 63 program stars (7 from Group A and 56 from Group B) are listed in Table 3.

It should be remarked here that a fraction of the Group B spectra (9 stars) may be problematic in the sense that lines in the short-wavelength region appear unusually weaker than expected (designated as "stars with weak broad Ca II K line" in Takeda 2020). Since different echelle orders are closely packed and the count level is considerably low in the blue-violet region of BOES spectra, this effect might be due to the stray light within the spectrograph. Accordingly, the results derived for those stars (marked with parentheses and asterisks in Table 3) should be viewed with caution.

**Table 2.** Basic information of the adopted observational data.

| Group | Instr. | Obs. Time | Resolution | Applied lines | Reference |
|-------|--------|-----------|------------|---------------|-----------|
| A | HIDES | 2017 Oct | 100000 | 3944/3961/ /3900/4663 | see Sect. 3.1 |
| B | BOES | 2008 Jan/Sep, 2009 Jan | 45000 | 3944/3961/6696/ /6698/4663 | Takeda et al. (2008, 2009) |
| C | HIDES | 2008 Oct | 100000 | 6696/6698/4663 | Takeda et al. (2012) |
| D | HIDES | 2006 May | 100000 | 4663 | Takeda et al. (2007) |

The group, to which the observational data adopted for each star belongs, is indicated in Table 3/tableE1.dat (3944/3961 lines; A or B), tableE2.dat (6696/6698 lines; B or C), tableE3.dat (3900 line; A), and tableE4.dat (4663 line; A or B or C or D).

---

[4] IRAF is distributed by the National Optical Astronomy Observatories, which is operated by the Association of Universities for Research in Astronomy, Inc. under cooperative agreement with the National Science Foundation.

**Table 3.** Program stars and their atmospheric parameters.

| HD# (1) | Name (2) | Sp.Type (3) | $T_{\rm eff}$ (4) | $\log g$ (5) | [Fe/H] (6) | $\xi$ (7) | $v_{\rm e} \sin i$ (8) | Group (9) | SB/V (10) | CP (11) | Hyades (12) |
|---|---|---|---|---|---|---|---|---|---|---|---|
| 018454 | 4 Eri | A5IV/V | 7740 | 4.07 | +0.24 | 3.9 | 100 | B | V | | |
| 076543 | $o^1$ Cnc | A5III | 8330 | 4.18 | +0.38 | 3.9 | 91 | B | SB | | |
| 012216 | 50 Cas | A2V | 9553 | 3.90 | +0.15 | 2.6 | 88 | B | SB2 | | |
| 028355 | 79 Tau | A7V | 7809 | 3.98 | +0.19 | 4.0 | 87 | B | V? | | H |
| 222345 | $\omega^1$ Aqr | A7IV | 7487 | 3.88 | −0.07 | 3.8 | 86 | B | SB | | |
| 074198 | $\gamma$ Cnc | A1IV | 9381 | 4.11 | +0.25 | 2.8 | 85 | B | SB | | |
| 027934 | $\kappa^1$ Tau | A7IV-V | 8159 | 3.84 | +0.02 | 4.0 | 83 | B | SB? | | H |
| 025490 | $\nu$ Tau | A1V | 9077 | 3.93 | −0.05 | 3.2 | 82 | B | | | |
| 029388 | 90 Tau | A6V | 8194 | 3.88 | −0.01 | 4.0 | 82 | B | SB1 | | H |
| 079469 | $\theta$ Hya | B9.5V | 10510 | 4.20 | −0.02 | 1.4 | 82 | B | SB | | |
| 028226 | | Am | 7361 | 4.01 | +0.31 | 3.6 | 81 | B | SB2 | Am | H |
| 207098 | $\delta$ Cap | A5mF2 (IV) | 7312 | 4.06 | +0.21 | 3.6 | 81 | B | SBo | Am | |
| 033641 | $\mu$ Aur | A4m | 7961 | 4.21 | +0.18 | 4.0 | 79 | B | V | Am | |
| 216627 | $\delta$ Aqr | A3V | 8587 | 3.59 | −0.25 | 3.7 | 79 | B | V | | |
| 012111 | 48 Cas | A3IV | 7910 | 4.08 | −0.23 | 4.0 | 76 | B | SBo | | |
| (*023281) | | A5m | 7761 | 4.19 | +0.05 | 4.0 | 76 | B | | Am | |
| 192640 | 29 Cyg | A2V | 8845 | 3.86 | −1.41 | 3.5 | 74 | B | V | $\lambda$ Boo | |
| 011636 | $\beta$ Ari | A5V... | 8294 | 4.12 | +0.15 | 3.9 | 73 | B | SBo | | |
| 005448 | $\mu$ And | A5V | 8147 | 3.82 | −0.14 | 4.0 | 72 | B | | | |
| 173880 | 111 Her | A5III | 8567 | 4.27 | +0.22 | 3.8 | 72 | B | SB? | | |
| 017093 | 38 Ari | A7III-IV | 7541 | 3.95 | −0.23 | 3.8 | 69 | B | V | | |
| 028319 | $\theta^2$ Tau | A7III | 7789 | 3.68 | −0.13 | 4.0 | 68 | B | SB1o | | H |
| 095382 | 59 Leo | A5III | 8017 | 3.95 | −0.09 | 4.0 | 68 | B | | | |
| (*140436) | $\gamma$ CrB | A1Vs | 9274 | 3.89 | −0.27 | 3.0 | 68 | B | | | |
| 020320 | $\zeta$ Eri | A5m | 7505 | 3.91 | −0.12 | 3.8 | 67 | B | SBo | Am | |

**Table 3.** Continued.

| HD# (1) | Name (2) | Sp.Type (3) | $T_{\mathrm{eff}}$ (4) | $\log g$ (5) | [Fe/H] (6) | $\xi$ (7) | $v_{\mathrm{e}} \sin i$ (8) | Group (9) | SB/V (10) | CP (11) | Hyades (12) |
|---|---|---|---|---|---|---|---|---|---|---|---|
| 013161 | $\beta$ Tri | A5III | 7957 | 3.68 | $-0.32$ | 4.0 | 65 | B | SB2o | | |
| 027045 | $\omega^2$ Tau | A3m | 7552 | 4.26 | $+0.36$ | 3.8 | 62 | B | SB | Am | |
| 200499 | $\eta$ Cap | A5V | 8081 | 3.95 | $-0.17$ | 4.0 | 62 | B | V | | |
| (*029499) | | A5m | 7638 | 4.08 | $+0.29$ | 3.9 | 61 | B | V | Am | H |
| 116656 | $\zeta$ UMa | A2V | 9317 | 4.10 | $+0.28$ | 2.9 | 59 | B | SB2o | | |
| 198639 | 56 Cyg | A4me... | 7921 | 4.09 | $+0.02$ | 4.0 | 59 | B | V? | Am | |
| (*130841) | $\alpha^2$ Lib | A3IV | 8079 | 3.96 | $-0.24$ | 4.0 | 58 | B | SB | | |
| 030121 | 4 Cam | A3m | 7700 | 3.98 | $+0.27$ | 3.9 | 57 | B | | Am | |
| 029479 | $\sigma^1$ Tau | A4m | 8406 | 4.14 | $+0.35$ | 3.9 | 56 | B | SBo | Am | H |
| 030210 | | Am... | 7927 | 3.94 | $+0.40$ | 4.0 | 56 | B | SB1? | Am | H |
| 222603 | $\lambda$ Psc | A7V | 7757 | 3.99 | $-0.17$ | 4.0 | 56 | B | SB | | |
| 212061 | $\gamma$ Aqr | A0V | 10384 | 3.95 | $-0.08$ | 1.5 | 54 | B | SB | | |
| 089021 | $\lambda$ UMa | A2IV | 8861 | 3.61 | $+0.08$ | 3.5 | 52 | B | V | | |
| 195725 | $\theta$ Cep | A7III | 7816 | 3.74 | $+0.16$ | 4.0 | 49 | B | SB2o | | |
| 043378 | 2 Lyn | A2Vs | 9210 | 4.09 | $-0.15$ | 3.0 | 46 | B | V? | | |
| 027819 | $\delta^2$ Tau | A7V | 8047 | 3.95 | $-0.05$ | 4.0 | 45 | B | SB | | H |
| 095418 | $\beta$ UMa | A1V | 9489 | 3.85 | $+0.24$ | 2.7 | 44 | B | SB | | |
| (*218396) | | A5V | 7091 | 4.06 | $-0.59$ | 3.3 | 41 | B | | | |
| 084107 | 15 Leo | A2IV | 8665 | 4.31 | $+0.01$ | 3.7 | 38 | B | | | |
| 204188 | | A8m | 7622 | 4.21 | $+0.02$ | 3.9 | 36 | B | SBo | Am | |
| (*033204) | | A5m | 7530 | 4.06 | $+0.18$ | 3.8 | 34 | B | | Am | H |
| 141795 | $\epsilon$ Ser | A2m | 8367 | 4.24 | $+0.25$ | 3.9 | 32 | B | V | Am | |
| 173648 | $\zeta^1$ Lyr | Am | 8004 | 3.90 | $+0.32$ | 4.0 | 32 | B | SB1o | Am | |
| (*027628) | 60 Tau | A3m | 7218 | 4.05 | $+0.10$ | 3.5 | 30 | B | SB1o | Am | H |

**Table 3.** Continued.

| HD# (1) | Name (2) | Sp.Type (3) | $T_{\mathrm{eff}}$ (4) | $\log g$ (5) | [Fe/H] (6) | $\xi$ (7) | $v_{\mathrm{e}} \sin i$ (8) | Group (9) | SB/V (10) | CP (11) | Hyades (12) |
|---|---|---|---|---|---|---|---|---|---|---|---|
| 028546 | 81 Tau | Am | 7640 | 4.17 | +0.23 | 3.9 | 28 | B | V? | Am | H |
| 182564 | $\pi$ Dra | A2IIIs | 9125 | 3.80 | +0.39 | 3.1 | 27 | A | | | |
| 172167 | $\alpha$ Lyr | A0Vvar | 9435 | 3.99 | $-0.53$ | 2.7 | 22 | A | V | $\lambda$ Boo? | |
| 060179 | $\alpha$ Gem | A2Vm | 9122 | 3.88 | $-0.02$ | 3.2 | 19 | B | SB1o | Am | |
| 058142 | 21 Lyn | A1V | 9384 | 3.74 | $-0.05$ | 2.8 | 19 | A | V | | |
| 095608 | 60 Leo | A1m | 8972 | 4.20 | +0.31 | 3.3 | 18 | B | | Am | |
| 048915 | $\alpha$ CMa | A0m... | 9938 | 4.31 | +0.45 | 2.1 | 17 | A | SBo | Am | |
| (*027749) | 63 Tau | A1m | 7448 | 4.21 | +0.41 | 3.7 | 13 | B | SB1o | Am | H |
| (*033254) | 16 Ori | A2m | 7747 | 4.14 | +0.28 | 3.9 | 13 | B | SBo | Am | H |
| 072037 | 2 UMa | A2m | 7918 | 4.16 | +0.19 | 4.0 | 12 | B | | Am | |
| 040932 | $\mu$ Ori | Am... | 8005 | 3.93 | $-0.12$ | 4.0 | 11 | B | SB1o | Am | H |
| 027962 | $\delta^3$ Tau | A2IV | 8923 | 3.94 | +0.25 | 3.4 | 11 | A | SB | | H |
| 047105 | $\gamma$ Gem | A0IV | 9115 | 3.49 | $-0.03$ | 3.2 | 11 | A | SB | | |
| 214994 | $o$ Peg | A1IV | 9453 | 3.64 | +0.18 | 2.7 | 6 | A | V | | |

(1) HD number. Regarding those parenthesized with asterisks (9 stars), caution should be taken because their observational data may be unreliable (cf. Sect. 3.1). (2) Bayer/Flamsteed name. (3) Spectral type taken from Hipparcos catalogue (ESA 1997). (4) Effective temperature (in K). (5) Logarithmic surface gravity ($\log g$ in dex, where $g$ is in unit of cm s$^{-2}$). (6) Differential Fe abundance relative to Procyon ($\simeq$ Sun) derived as $A$(Fe) $-7.49$. (7) Microturbulent velocity (in km s$^{-1}$). (8) Projected rotational velocity (in km s$^{-1}$). (9) Data source group used for the analysis of Al i 3944/3961 lines (cf. Table 2). (10) Key to spectroscopic binary (SB, "o" denotes the case where orbital elements are available) or radial velocity variable (V). (11) Key to chemical peculiarity type (Am or $\lambda$ Boo), where the spectral classifications in three sources were consulted: Hipparcos catalogue (ESA 1997), Bright Star Catalogue (Hoffleit, Jaschek 1991), and SIMBAD. (12) Key to membership of Hyades cluster (H). Since these data (arranged in the descending order of $v_{\mathrm{e}} \sin i$) are essentially the subset of those used in Takeda et al. (2018), the caption of Table 1 of that paper may be consulted for more details.

## 3.2. Atmospheric parameters

The atmospheric parameters of the program stars are presented in Table 3, which are the same as determined and adopted in Takeda et al. (2008, 2009). Since only brief descriptions are given here, these papers should be consulted for more details: $T_{\rm eff}$ and $\log g$ are from Strömgren's $uvby\beta$ color indices by using Napiwotzki et al.'s (1993) calibration, $\xi$ is from the empirical $T_{\rm eff}$-dependent relation [cf. Eq.(1) of Takeda et al. 2008], and [Fe/H] (Fe abundance, representative of the metallicity) is from the spectrum fitting analysis in the 6140–6170 Å region.
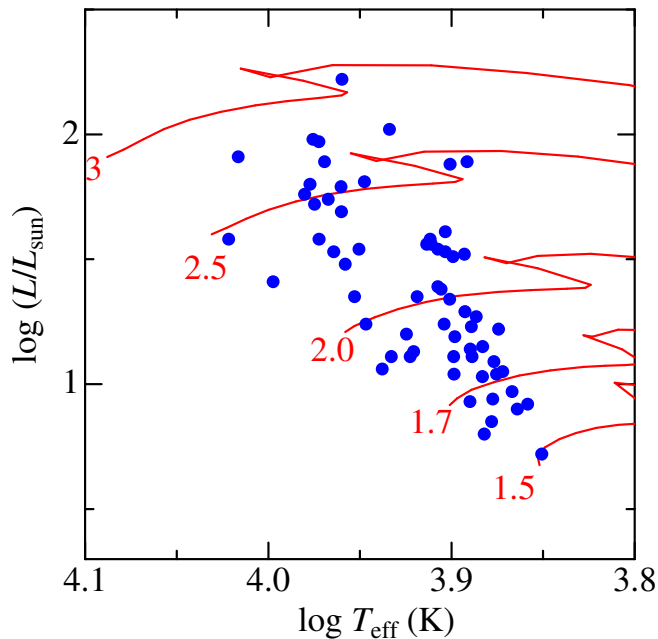


**Figure 6.** Our program stars plotted on the $\log(L/L_\odot)$ vs. $\log T_{\rm eff}$ diagram, where $L$ (luminosity) was evaluated from visual magnitude (corrected for interstellar extinction by following Arenou et al. 1992), Hipparcos parallax (van Leeuwen 2007), and bolometric correction (Flower 1996). Lejeune and Schaerer's (2001) theoretical solar-metallicity tracks for 5 different masses (1.5, 1.7, 2, 2.5, and 3 $M_\odot$) are also depicted by solid lines for comparison.

The model atmosphere for each star was generated by interpolating Kurucz's (1993) ATLAS9 grid of models in terms of $T_{\rm eff}$, $\log g$, and [Fe/H]. Likewise, the depth-dependent non-LTE departure coefficients to be used for each of the program stars were obtained by interpolation of the calculated grids (Sect. 2.1) with respect to $T_{\rm eff}$, $\log g$, and [Fe/H].

The 63 program stars are plotted on the $\log T_{\mathrm{eff}}$ vs. $\log L$ diagram in Fig. 6, where the theoretical evolutionary tracks of different masses are also depicted for comparison. We can see from this figure that these stars are in the mass range of $1.5 M_\odot \lesssim M \lesssim 3 M_\odot$.
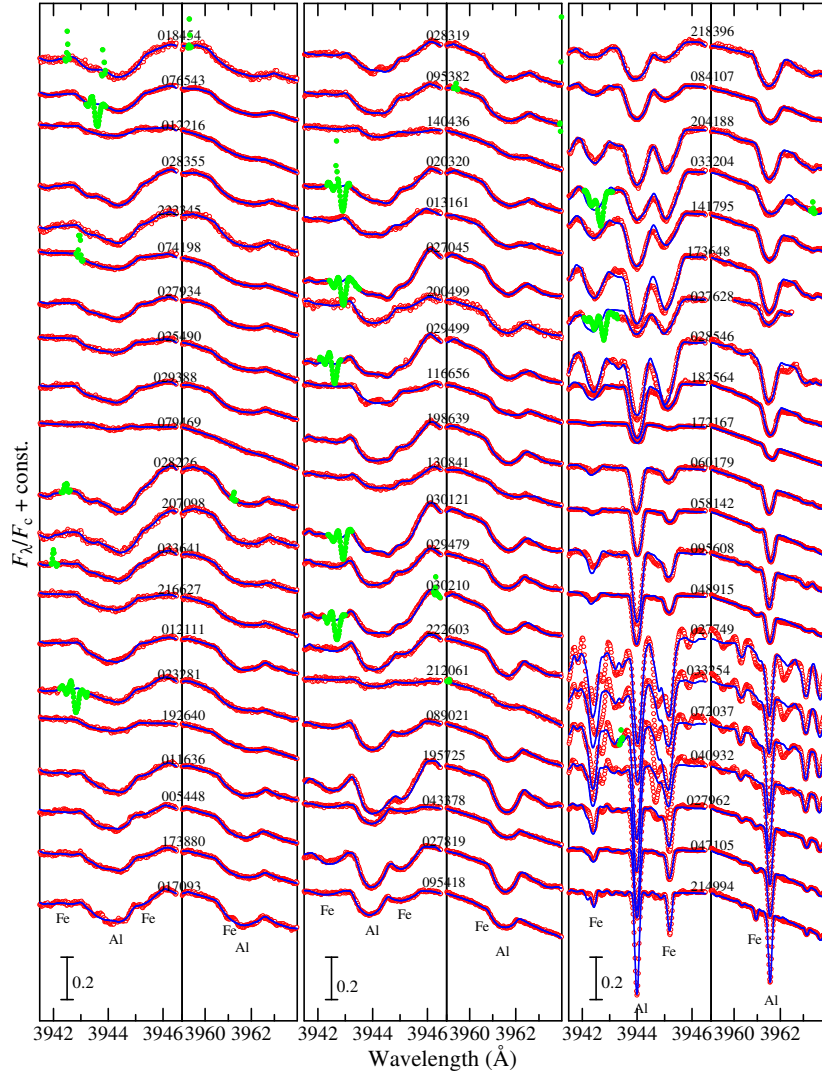
### 3.3. Abundance determination

The abundances of Al for each of the 63 stars were determined in the similar manner as done in the previous papers (Takeda et al. 2008, 2009, 2018; Takeda 2022). (i) First, Takeda's (1995) spectrum-fitting technique is applied to each of the spectral regions comprising Al I 3944 and 3961 lines, while varying several free parameters ($v_{\mathrm{e}} \sin i$, radial velocity, and abundances of important elements; see Table 4 for more information), and the best fit parameter solutions are determined. (ii) Then, based on such established abundance solutions, the equivalent widths of these two Al lines ($W$) were inversely calculated. (iii) Finally, non-LTE ($A^{\mathrm{N}}$) and LTE ($A^{\mathrm{L}}$) abundances were derived from $W$, along with the corresponding non-LTE correction $\Delta (\equiv A^{\mathrm{N}} - A^{\mathrm{L}})$. The accomplished fit between the theoretical and observed spectra is displayed for each region in Fig. 7, and the results of the analysis ($W$, $A^{\mathrm{N}}$, $A^{\mathrm{L}}$, $\Delta$) for each line are summarized in "tableE1.dat" of the supplementary materials.

**Table 4.** Details of spectrum fitting analyses.

| Lines | Fitting (Å) range (Å) | Abundances varied* | Targets | Figure |
|:---:|:---:|:---:|:---:|:---:|
| Al I 3944 | 3941.5–3946.5 | Al, Fe | All 63 stars | Fig. 7 |
| Al I 3961 | 3859–3964 | Al, Fe | All 63 stars | Fig. 7 |
| Al I 6696/6698 | 6692–6701 | Al, Fe | 8 sharp-lined late-A stars | Fig. 11a |
| Al II 3900 | 3898.5–3902 | Al, Ti, V, Fe | 6 sharp-lined early-A stars | Fig. 11c |
| Al II 4663 | 4662–4665 | Al, Fe | 10 sharp-lined early-A stars | Fig. 11e |

* The abundances of other elements than these were fixed by assuming [X/H] = [Fe/H] in the fitting.

The resulting $W_{3944}$, $\Delta_{3944}$, and $A^{\mathrm{N}}_{3944}$ along with the abundance sensitivities to typical ambiguities in atmospheric parameters [$\delta_{T\pm}$ (abundance changes for $T_{\mathrm{eff}}$ perturbations by $\pm 3\%$), $\delta_{g\pm}$ (abundance changes for $\log g$ perturbations by $\pm 0.1$ dex), and $\delta_{\xi\pm}$ (abundance changes for $\xi$ perturbations by $\pm 30\%$)] are plotted against $T_{\mathrm{eff}}$ in Fig. 8. (Although the results only for the Al I 3944 line are shown here, those for the 3961 line are quite similar.) Fig. 8a and 8b confirm the trends of $W$ and $\Delta$ already described in Sect. 2.4. It can be seen also from Fig. 8d and 8f that Al abundances derived from these strong resonance lines are quite sensitive to $T_{\mathrm{eff}}$ and especially to $\xi$, as expected.

**Figure 7.** Synthetic spectrum-fitting analysis for Al abundance determinations from Al I 3944/3961 lines, The best-fit theoretical spectra (in the selected ranges of 3941.5–3946.5 Å and 3959–3964 Å comprising the relevant Al I lines) are depicted by blue solid lines, while the observed data are plotted by red symbols (the masked data excluded in judging the goodness of the fit are highlighted in green). In each panel, the spectra (residual fluxes $F_\lambda/F_c$; the spectrum at 3946.5 Å in the left and that at 3959 Å in the right are so adjusted as to coincide with each other) are arranged in the descending order of $v_e \sin i$ (from left to right, from top to bottom). An appropriate offset is applied to each spectrum (indicated by the HD number) relative to the adjacent one. The wavelength scale is in the laboratory frame after correcting the radial velocity shift.
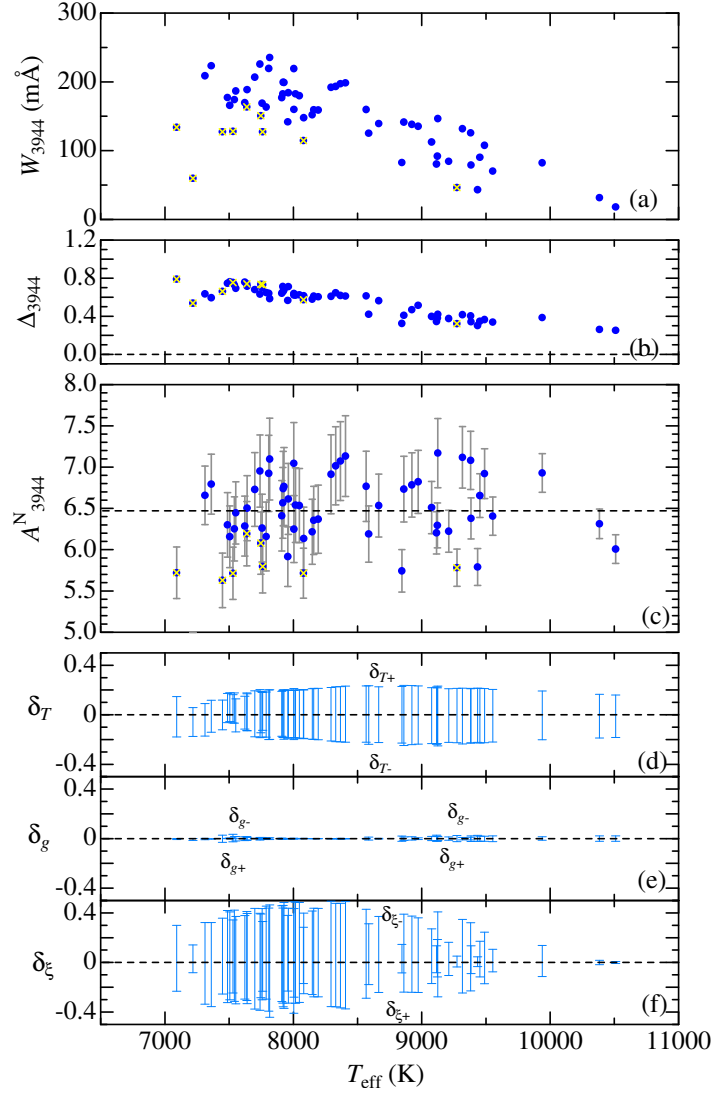
**Figure 8.** Al abundances and the related quantities of the program stars, which were derived from the Al I 3944 line, are plotted against $T_{\rm eff}$. (a) Equivalent widths ($W_{3944}$, filled symbols). (b) Non-LTE corrections ($\Delta_{3944}$, filled symbols). (c) $A^{\rm N}_{3944}$ (non-LTE Al abundances), where the adopted solar abundance ($A_\odot = 6.47$) is indicated by the horizontal dashed line and the error bar denotes $\pm\delta_{Tgv}$ defined as the root-sum-square of $\delta_T$, $\delta_g$, and $\delta_\xi$ (e.g., $\delta_T$ is the mean of $|\delta_{T+}|$ and $|\delta_{T-}|$; etc.). (d) $\delta_{T+}$ and $\delta_{T-}$ (abundance variations in response to $T_{\rm eff}$ changes of $+3\%$ and $-3\%$). (e) $\delta_{g+}$ and $\delta_{g-}$ (abundance variations in response to $\log g$ changes by $+0.1$ dex and $-0.1$ dex). (f) $\delta_{\xi+}$ and $\delta_{\xi-}$ (abundance variations in response to perturbing $\xi$ by $+30\%$ and $-30\%$). The results based on unreliable observational data (cf. Sect. 3.1) are distinguished by overplotting yellow crosses in panels (a)–(c).
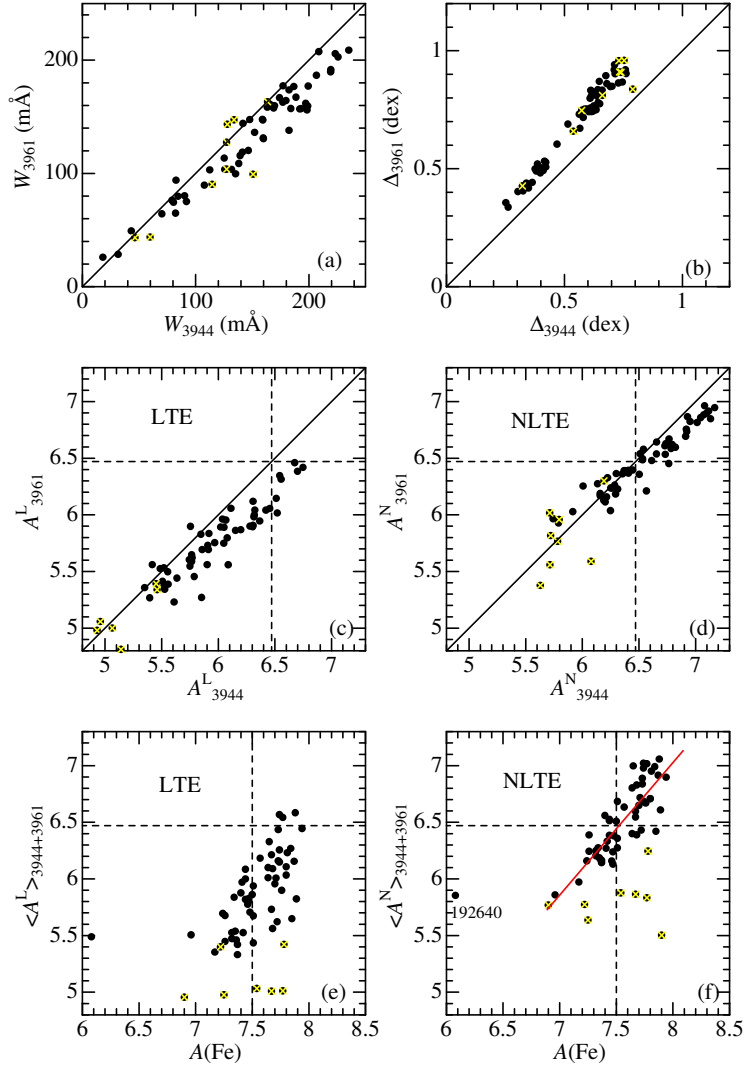
**Figure 9.** Panels (a)–(d) show the correlations of the quantities between Al I 3944 and 3961 lines (a: equivalent widths, b: NLTE corrections, c: LTE abundances, and d: NLTE abundances). The mean Al abundances derived from Al I 3944/3961 lines, defined as $\langle A \rangle_{3944+3961} \equiv (A_{3944}+A_{3961})/2$, are plotted against $A(\mathrm{Fe})$ (= [Fe/H] + 7.49; cf. Table 1) in panel (e; LTE) and panel (f; NLTE). The results based on unreliable observational data (cf. Sect. 3.1) are distinguished by overplotting yellow crosses as in Fig. 8. In each panel, the locations of solar abundances are indicated by dashed lines. The solid line in panels (a)–(d) is the guide line corresponding to $X_{3944} = X_{3961}$ ($X$ is $\Delta$ or $A$), while the red solid line depicted in panel (f) is the linear-regression line showing the main trend (cf. Sect. 3.4).

### 3.4. Results and their characteristics

The abundances and related quantities resulting from the analysis of the Al $\mathrm{I}$ 3944/3961 lines are graphically depicted in Fig. 9, from which the following trends are observed.

– While the equivalent widths of these doublet lines ($W_{3944}$ and $W_{3961}$) are not much different from each other (Fig. 9a), the non-LTE corrections generally satisfy the inequality relation $(0 <)\Delta_{3944} < \Delta_{3961}$ (Fig. 9b), as already mentioned in Sect. 2.4.

– Although $A^{\mathrm{L}}_{3944}$ tends to be systematically higher than $A^{\mathrm{L}}_{3961}$ in the LTE case (Fig. 9c), this discrepancy is mitigated by the difference in $\Delta$ to result in $A^{\mathrm{N}}_{3944} \approx A^{\mathrm{N}}_{3961}$ in the non-LTE case (Fig. 9d).

– In terms of the averaged abundance between two lines, $\langle A \rangle_{3944+3961} \equiv (A_{3944} + A_{3961})/2$, while the LTE abundances ($\langle A^{\mathrm{L}} \rangle_{3944+3961}$) are considerably subsolar around the solar metallicity (Fig. 9e), this discordance is satisfactorily removed in the non-LTE case ($\langle A^{\mathrm{N}} \rangle_{3944+3961}$), so that normal-metallicity stars reasonably show $A_{\mathrm{star}} \sim A_{\odot}$ for both Al and Fe (Fig. 9f).

– By applying the least-squares analysis to the data in Fig. 9f (while excluding those yellow-crossed unreliable ones and that of the $\lambda$ Boo star HD 192640 showing exceptionally low metallicity of [Fe/H]$= -1.41$), the linear-regression relation [Al/H] $= 1.17(\pm 0.11)$ [Fe/H] $-0.04(\pm 0.03)$ is obtained, where [Al/H] $= A(\mathrm{Al}) -6.47$ and [Fe/H] $= A(\mathrm{Fe}) -7.49$.

– The scaling relation ([Al/H] $\sim 1.2$ [Fe/H]) observationally established here indicates that an overabundance of Al is associated with an increased Fe abundance in the surface of A-type stars. This trend is qualitatively consistent with the prediction from the diffusion theory, which suggests an abundance excess of Al (like Fe) as a result of the element segregation process in the envelope of Am stars (Richer et al. 2000; Talon et al. 2006).

### 3.5. Interpretation of the problems in previous studies

It is now possible to discuss the problematic issues seen in the old Al abundance determinations for A-type stars based on the Al $\mathrm{I}$ resonance doublet lines.

The serious zero-point discrepancy in [Al/H] (considerably negative [Al/H] values for [Fe/H] $\sim$ 0 stars) seen in the Al abundances derived from Al $\mathrm{I}$ 3944/3961 lines by Smith (1971, 1973) and Adelman (et al.) in 1980s–90s (cf. Figs. 2a and 2c) is simply because they adopted LTE in their analysis. Since appreciable (positive) non-LTE corrections due to Al $\mathrm{I}$ overionization are required, LTE Al abundances are significantly underestimated and shifted towards subsolar direction (Fig. 9e). This problem can be reasonably resolved by taking into account the non-LTE effect as shown in Fig. 9f.

The systematic discrepancy in the LTE abundances between Al I 3944 and 3961 lines seen in Adelman et al.'s results ($A_{3944} > A_{3961}$; cf. Fig. 2d) may also be associated to the non-LTE effect, because neglecting non-LTE corrections ($\Delta_{3944} < \Delta_{3961}$) results in such a tendency as shown in Fig. 9c. However, the extent of discordance observed in Fig. 2d seems to be larger than that expected from Fig. 9c. As another possibility, they might have not included the opacity of Balmer line wings, the neglect of which can cause appreciable abundance differences because the 3961 line is more affected by this effect (due to H$\epsilon$ at 3970 Å) than the 3944 line, as demonstrated in Fig. 10. Therefore, in order to derive correct Al abundances from the Al I 3944/3961 lines, it is mandatory to take into account not only the non-LTE effect but also the background Balmer line opacities.
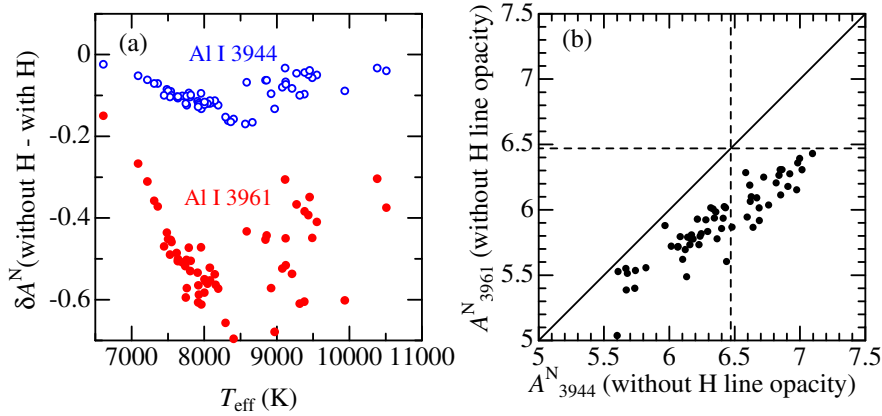


**Figure 10.** (a) The values of $\delta A^{\mathrm{N}}$ (abundance difference of two $A^{\mathrm{N}}$ values obtained by neglecting and correctly including the overlapping opacity of Balmer line wings) are plotted against $T_{\mathrm{eff}}$. Open and filed symbols correspond to Al I 3944 and 3961 lines, respectively. (b) Correlation plots between $A_{3944}^{\mathrm{N}}$(without H line) and $A_{3961}^{\mathrm{N}}$(without H line), which should be compared with Fig. 9d (results derived by correctly including the H line opacity).

## 4. Other aluminium lines as abundance indicators

Finally, some discussion may be in order regarding whether and how other lines (than Al I 3944/3961 doublet) are applicable to determining Al abundances of A-type stars. Here, three candidate lines were examined: Al I 6696/6698, Al II 3900, and Al II 4663. It turned out, however, that abundances could be derived for only a limited number ($\lesssim 10$ for each line) of sharp-line stars ($v_{\mathrm{e}} \sin i$ less than several tens km s$^{-1}$) because these lines are generally weak.

Accordingly, abundance determinations (such as done in Sect. 3.3) were carried out for 8 mostly late A-type stars (Al I 6696/6698), 6 early A-type stars (Al II 3900), and 10 early A-type stars (Al II 4663). The adopted line data are given in Table 1, and the details of spectrum fittings are presented in Table 4. The results ($W$, $A^{\mathrm{N}}$, $A^{\mathrm{L}}$, $\Delta$) are summarized in "tableE2.dat" (6696),[5] "tableE3.dat" (3900), and "tableE4.dat" (4663) of the supplementary materials. The accomplished fit for each region and the correlations of the resulting non-LTE Al abundances ($A^{\mathrm{N}}_{6696}$, $A^{\mathrm{N}}_{3900}$, and $A^{\mathrm{N}}_{4663}$) with $\langle A^{\mathrm{N}} \rangle_{3944+3961}$ are displayed in Fig. 11.

Regarding the high-excitation Al I 6696 line, which was also used by Burkhart and Coupry (1989, 1991, 2000) for their study of lower $T_{\mathrm{eff}}$ ($\lesssim 8000$ K) stars, $A^{\mathrm{N}}_{6696}$ is more or less consistent with $\langle A^{\mathrm{N}} \rangle_{3944+3961}$ (Fig. 11b), if unreliable (yellow-crossed) data and that of HD 047105 (the very weak-line case with $W_{6696}$ of only 1.2 mÅ) are excluded. It should be noted that positive non-LTE corrections of $\Delta \sim 0.1$–0.3 dex are expected for this line, though comparatively less significant than in the case of Al I 3944/3961.

Rather disappointingly, the Al II 3900.675 line was found to be badly blended with the neighboring much stronger Ti II 3900.539 line, as shown in Fig. 11c. While Al abundances could be somehow determined in this synthetic fitting analysis by making use of the slight asymmetry in the blended feature, the resulting $A^{\mathrm{N}}_{3900}$ turned out to be systematically lower than $\langle A^{\mathrm{N}} \rangle_{3944+3961}$ (Fig. 11d); the reason for this discrepancy is not clear. In any event, this Al II 3900 line is not suitable for abundance determination, despite that it is unaffected by any non-LTE effect ($|\Delta| \lesssim 0.01$ dex, its sign is positive or negative).

In contrast, the other Al II line at 4663 Å is much more favorable, which is almost free from any blending (Fig. 11e). Actually, $A^{\mathrm{N}}_{4663}$ and $\langle A^{\mathrm{N}} \rangle_{3944+3961}$ are in satisfactory agreement with each other (though one exception is HD 060179) as seen in Fig. 11f. Since the non-LTE correction is negligibly small ($\Delta \lesssim 0.02$ dex; $\Delta$ is positive), it may be analyzed with the assumption of LTE. This Al II 4663 line would serve as a good Al abundance indicator for early A- through late B-type stars, as long as it is measurable.

## 5. Summary and conclusion

Although various abundance anomalies are known to be observed in the surface of A-type stars on the upper main sequence (e.g., Am stars), the behavior of aluminium abundances is still poorly understood, for which even the qualitative trend (excess or deficiency in Am stars) is not established.

That is, according to the past work on Al abundances of A stars, for which the strong resonance Al I 3944/3961 lines were mostly employed, [Al/H] tends to be considerably negative for stars of near-normal metallicity ([Fe/H] $\sim 0$),

---

[5]Although the fitting was done in the wavelength region including both 6696 and 6698 lines, only the results for the 6696 line (twice as strong as the 6698 line) are presented here.
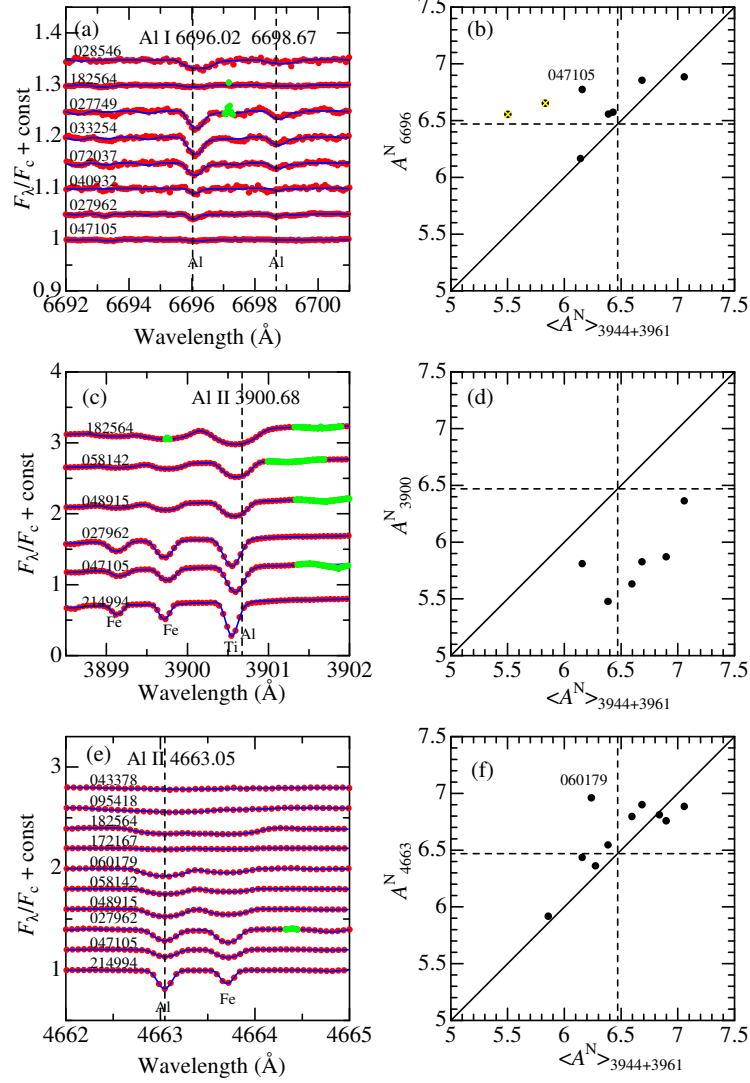
**Figure 11.** The left-hand panels (a, c, e) show the accomplished fit of synthetic spectrum analysis carried out for determining the abundances of Al by using (a) Al I 6696/6698 (6692–6701 Å region) (c) Al II 3900 (3898.5–3902 Å region), and (e) Al II 4663 (4662–4665 Å region). The wavelength positions of the relevant Al lines are shown by vertical dashed lines. Otherwise, the meanings of the lines and symbols are the same as in Fig. 7. The non-LTE Al abundances ($A^N$) resulting from these three regions are plotted against $\langle A^N \rangle_{3944+3961}$ (mean NLTE abundances of those derived from Al I 3944/3961 lines) in the corresponding right-hand panels (b, d, f), respectively. Yellow crosses are overplotted on the results based on unreliable observational data as in Fig. 9.

despite that $A(\mathrm{Al})$ appears to be positively correlated with $A(\mathrm{Fe})$. Moreover, the reported Al abundances derived from 3944 and 3961 lines were not consistent with each other.

This is presumably related to the fact that these previous Al abundance determinations were done with the assumption of LTE, despite that considerable non-LTE corrections are suspected for these Al I lines. Unfortunately, however, the impact of the non-LTE effect on Al abundance determination of A-type stars in general has barely been investigated so far.

With an aim to shed light on this issue, extensive statistical-equilibrium calculations on Al I/Al II were carried out for a wide range of atmospheric parameters covering early F- to late B-type main-sequence stars (6500–14000 K in $T_{\mathrm{eff}}$, 3.0–4.5 in $\log g$, and $-1.0$ to $+0.5$ in [Fe/H]), and the equivalent widths ($W$) and non-LTE abundance corrections ($\Delta$) for these 3944 and 3961 lines were then calculated for these model grids, which are presented as supplementary materials.

These calculations revealed that these Al I resonance doublet lines are considerably weakened by the non-LTE effect due to the overionization mechanism, which means that $\Delta$ values are always positive and significantly large ($0.3 \lesssim \Delta \lesssim 1.0$ dex) and tending to increase with $W$ (or with a decrease in $T_{\mathrm{eff}}$), where an inequality relation of $\Delta_{3944} < \Delta_{3961}$ generally holds.

As a practical application of these results, non-LTE Al abundances were determined by applying the spectrum-fitting technique to the Al I 3944/3961 lines for selected 63 A-type dwarfs ($7000 \lesssim T_{\mathrm{eff}} \lesssim 10000$ K) of comparatively lower rotational velocities ($v_{\mathrm{e}} \sin i \lesssim 100$ km s$^{-1}$) based on the high-dispersion spectra obtained at the Okayama Astrophysical Observatory and the Bohyunsan Optical Astronomy Observatory.

It then turned out that consistent non-LTE abundances for both lines could be obtained and resulted in [Al/H] $\sim$ [Fe/H] $\sim 0$ for normal metallicity stars, which means that the serious zero-point discrepancy found in old studies has been settled. This clearly indicates that applying the non-LTE corrections (and inclusion of Balmer line wings as background opacity) is indispensable for reliable Al abundance determinations of A-type stars from Al I 3944/3961 lines.

The resulting Al abundances of A-type stars are almost in proportion to [Fe/H] (tending to be overabundant in Am stars) with an approximate scaling relation of [Al/H] $\sim 1.2$ [Fe/H]. This consequence is qualitatively consistent with the prediction of the diffusion theory (suggesting an Al excess in the photosphere of Am stars).[6]

As a by-product of this study, the applicability of other Al lines (Al I 6696/6698, Al II 3900, and Al II 4663) for Al abundance determination of A-type stars was also investigated. The Al II 3900 line turned out to be un-

---

[6]It should be remarked, however, that the situation is different for HgMn stars (chemically peculiar stars in the regime of late B-type stars), for which Al tends to be deficient as separately described in Appendix A for the case of the AR Aur system.

suitable because it is badly blended with the strong Ti II 3900 line. Yet, the Al I 6696/6698 lines (for late A-type stars; with a mild non-LTE correction of 0.1–0.3 dex) and Al II 4663 line (for early A-type stars; almost free from the non-LTE effect) may be usable as Al abundance indicators, though limited to only sharp-lined stars because of their weakness.

## Online supplementary materials

The following electronic tables associated with this article are available at `https://www.astro.sk/caosp/Eedition/FullTexts/vol53no2/pp31-60.dat/`.

## References

Adelman S. J., 1984, MNRAS, 206, 637 [DOI: `10.1093/mnras/206.3.637`]

Adelman S. J., 1988, MNRAS, 230, 671 [DOI: `10.1093/mnras/230.4.671`]

Adelman S. J., 1994, MNRAS, 271, 355 [DOI: `10.1093/mnras/271.2.355`]

Adelman S. J., Caliskan H., Kocer D., Bolcal C., 1997, MNRAS, 288, 470 [DOI: `10.1093/mnras/288.2.470`]

Adelman S. J., Young J. M., Baldwin H. E., 1984, MNRAS, 206, 649 [DOI: `10.1093/mnras/206.3.649`]

Anders E., Grevesse N., 1989, Geochim. Cosmochim. Acta, 53, 197 [DOI: `10.1016/0016-7037(89)90286-X`]

Andrievsky S. M., Spite M., Korotin S. A., Spite F., Bonifacio P., Cayrel R., Hill V., François P., 2008, A&A, 481, 481 [DOI: `10.1051/0004-6361:20078837`]

Arenou F., Grenon M., Gómez A., 1992, A&A, 258, 104

Asplund M., Grevesse N., Sauval A. J., Scott P., 2009, ARA&A, 47, 481 [DOI: `10.1146/annurev.astro.46.060407.145222`]

Baumüller D., Gehren T., 1996, A&A, 307, 961

Baumüller D., Gehren T., 1997, A&A, 325, 1088

Burkhart C., Coupry M. F., 1989, A&A, 220, 197

Burkhart C., Coupry M. F., 1991, A&A, 249, 205

Burkhart C., Coupry M. F., 2000, A&A, 354, 216

Conti P. S., 1970, PASP, 82, 781 [DOI: `10.1086/128965`]

Cunto W., Mendoza C., 1992, Rev. Mex. Astron. Astrofis., 23, 107

ESA, 1997, The Hipparcos and Tycho Catalogues, ESA SP-1200, available from NASA-ADC or CDS in a machine-readable form (file name: `hip_main.dat`)

Ezzeddine R., Merle T., Plez B., Gebran M., Thévenin F., Van der Swaelmen M., 2018, A&A, 618, A141 [DOI: 10.1051/0004-6361/201630352]

Flower P. J., 1996, ApJ, 469, 355 [DOI: 10.1086/177785]

Folsom C. P., Kochukhov O., Wade G. A., Silvester J., Bagnulo S., 2010, MNRAS, 407, 2383 [DOI: 10.1111/j.1365-2966.2010.17057.x]

Grevesse N., Sauval A. J., 1999, A&A, 347, 348

Griem H. R., 1960, ApJ, 132, 883 [DOI: 10.1086/146987]

Griem H. R., 1967, ApJ, 147, 1092 [DOI: 10.1086/149097]

Hoffleit D., Jaschek C., 1991, The Bright Star Catalogue, 5th revised edition (New Haven, Conn.: Yale University Observatory)

Khokhlova V. L., Zverko Yu., Zhizhnovskii I., Griffin R. E. M., 1995, Astron. Lett., 21, 818

Kurucz R. L., 1993, Kurucz CD-ROM, No. 13 (Harvard-Smithsonian Center for Astrophysics)

Kurucz R. L., Bell B., 1995, Kurucz CD-ROM, No. 23 (Harvard-Smithsonian Center for Astrophysics)

Lambert D. L., Warner B., 1968, MNRAS, 138, 181 [DOI: 10.1093/mnras/138.2.181]

Lejeune T., Schaerer D., 2001, A&A, 366, 538 (DOI: 10.1051/0004-6361:20000214)

Mashonkina L., Zhao G., Gehren T., Aoki W., Bergemann M., Noguchi K., Shi J. R., Takada-Hidai M., Zhang H. W., 2008, A&A, 478, 529 [DOI: 10.1051/0004-6361:20078060]

Napiwotzki R., Schönberner D., Wenske V., 1993, A&A, 268, 653

Nordlander T., Lind K., 2017, A&A, 607, A75 [DOI: 10.1051/0004-6361/201730427]

Richer J., Michaud G., Turcotte S., 2000, ApJ, 529, 338 (DOI: 10.1086/308274)

Ryabchikova T., Piskunov N., Kurucz R. L., Stempels H. C., Heiter U., Pakhomov Yu., Barklem P. S., 2015, Phys. Scr., 90, 054005 [DOI: 10.1088/0031-8949/90/5/054005]

Smith K. C., 1993, A&A, 276, 393

Smith M. A., 1971, A&A, 11, 325

Smith M. A., 1973, ApJS, 25, 277 [DOI: 10.1086/190270]

Steenbock W., Holweger H., 1992, in The Atmospheres of Early-Type Stars, Lecture Notes in Physics, Volume 401 (Springer, Berlin), p. 57 [DOI: 10.1007/3-540-55256-1_280]

Takeda Y., 1991, A&A, 242, 455

Takeda Y., 1995, PASJ, 47, 287

Takeda Y., 2020, Stars and Galaxies, Vol.3, id.1 (http://www.nhao.jp/research/starsandgalaxies/03.html#2020J-1) [DOI: 10.48550/arXiv.2012.15152]

Takeda Y., 2022, Contr. Astron. Obs. Skalnaté Pleso, 52, 5 [DOI: 10.31577/caosp.2022.52.1.5]

Takeda Y., Han I., Kang D.-I., Lee B.-C., Kim K.-M., 2008, JKAS, 41, 83
(DOI: 10.5303/JKAS.2008.41.4.083)

Takeda Y., Han I., Kang D.-I., Lee B.-C., Kim K.-M., 2019, MNRAS, 485, 1067
[DOI: 10.1093/mnras/stz449]

Takeda Y., Kang D.-I., Han I., Lee B.-C., Kim K.-M., 2009, PASJ, 61, 1165
(DOI: 10.1093/pasj/61.5.1165)

Takeda Y., Kang D.-I., Han I., Lee B.-C., Kim K.-M., Kawanomoto S., Ohishi N.,
2012, PASJ, 64, 38 (DOI: 10.1093/pasj/64.2.38)

Takeda Y., Kawanomoto S., Ohishi N., 2007, PASJ, 59, 245
(DOI: 10.1093/pasj/59.1.245)

Takeda Y., Kawanomoto S., Ohishi N., Kang D.-I., Lee B.-C., Kim K.-M., Han I.,
2018, PASJ, 70, 91 (DOI: 10.1093/pasj/psy091)

Talon S., Richard O., Michaud G., 2006, ApJ, 645, 634 (DOI: 10.1086/504066)

van Leeuwen F., 2007, Hipparcos, the New Reduction of the Raw Data, Astrophysics
and Space Science Library, Vol. 350
(Berlin: Springer) (DOI: 10.1007/978-1-4020-6342-8)

## A. Aluminium abundances of the AR Aur system

In the author's previous non-LTE abundance determinations of CNO (covering up to $T_{\rm eff} \lesssim 11000$ K; Takeda et al. 2018) and of Si (up to $T_{\rm eff} \lesssim 14000$ K; Takeda 2022), which were based on the spectra obtained with HIDES and BOES like in this study, it was possible to derive the abundances of HgMn stars (an important group of chemically peculiar stars at 10000 K $\lesssim T_{\rm eff}$). Unfortunately, the program stars of this investigation could contain only A-type stars of $T_{\rm eff} \lesssim 10000$ K (and HgMn stars are lacking), because the HIDES data of late B-type stars used in the past studies do not include the short-wavelength region covering the Al I 3944/3961 lines.

However, a set of BOES spectra (of wide wavelength coverage) for AR Aur, a double-lined eclipsing binary comprising a HgMn star (primary [P], B9V) and a normal star (secondary [S], B9.5V), are available (Takeda et al. 2019). Therefore, as a supplementary analysis, non-LTE Al abundances of AR Aur (P) and AR Aur (S) were determined by applying the spectrum-fitting analysis to Al I 3944, Al I 3961, and Al II 4663 lines as done in Sect. 3.3, in order to check whether any difference exists in Al abundances between normal and HgMn stars. The spectra of both stars were disentangled as described in Sect. 2.2 of Takeda et al. (2019), and the same atmospheric parameters as well as model atmospheres as used in that paper were adopted.

The results are summarized in Table 5, and the accomplished spectrum fit in each region is shown in Fig. 12, from which the following consequences can be drawn.

- As seen from Fig. 12, the Al lines are very weak and hardly detectable in AR Aur (P), which means that reliable abundance determination is not feasible. Still, $A(\rm Al) \lesssim 5.5$ (i.e., [Al/H] $\lesssim -1$) may be concluded from Table 5 as the photospheric Al abundance for this HgMn star.

- In contrast, all three Al lines are clearly observable in AR Aur (S), and a near-solar abundance of $A(\rm Al) \simeq 6.6$ ([Al/H] $\simeq +0.1$) is consistently obtained for this normal B9.5V star.

- In summary, while the secondary star has quite normal abundances for both Fe and Al ([Fe/H] $\simeq$ [Al/H] $\simeq +0.1$), Al is considerably deficient in the primary HgMn star ([Al/H] $\lesssim -1$) despite that it is Fe-rich ([Fe/H]$= +0.5$).

- Two chemical abundance studies (including Al) on AR Aur based on LTE are already published. Khokhlova et al. (1995) derived [Al/H] $= -1.2$ (P) and $+0.5$ (S) from Al I 3944/3961 lines. Meanwhile, Folsom et al. (2010) concluded [Al/H] $= -1.37$ (P) and $+0.30$ (S) (though the adopted spectral lines are not explicitly described). While their results for the primary (marked Al deficiency by $\lesssim -1$ dex) are quite consistent with the consequence here, those for the secondary (moderate Al excess by several tenths dex) appear to be somewhat overestimated.

- Accordingly, unlike Am stars (for which Al-excess is accompanied with an overabundance of Fe), photospheric Al abundances in HgMn stars can be considerably deficient even for the case of supersolar Fe. This means that these two groups of chemically peculiar stars are markedly different as long as the behavior of Al abundance is concerned.

- This observational fact is a reconfirmation of the results of Smith (1993), who concluded from the analysis of UV lines based on IUE spectra that Al is deficient (becoming increasingly underabundant at higher $T_{\rm eff}$) in essentially all HgMn stars.
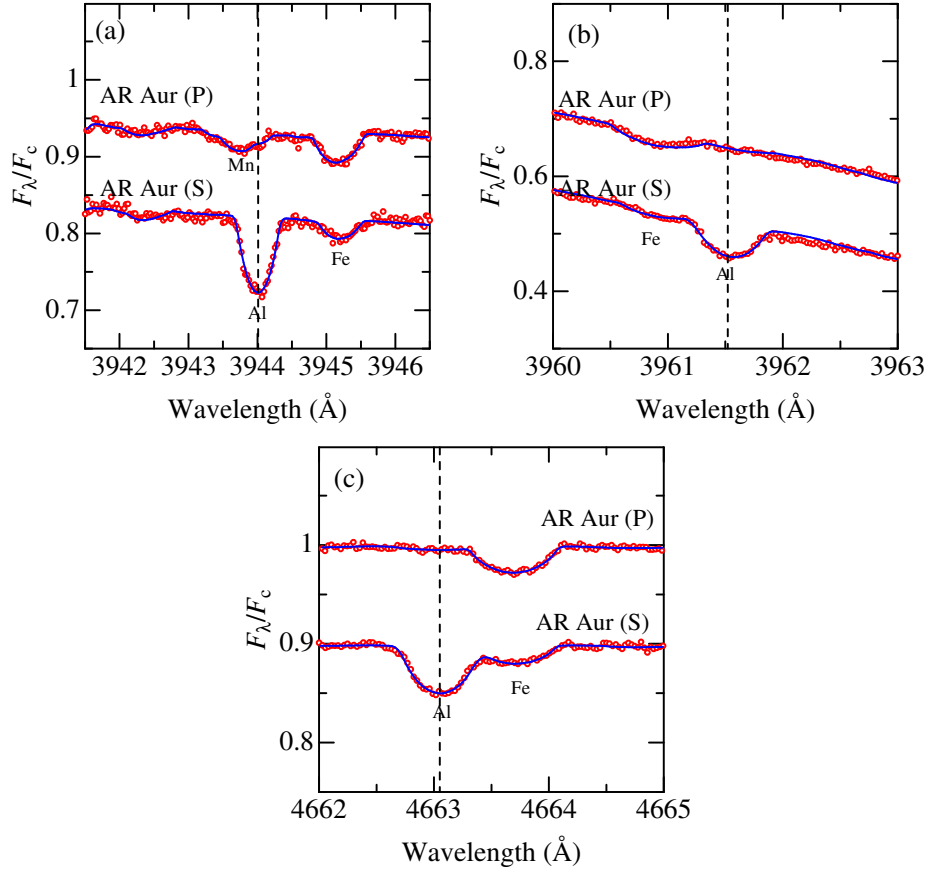
**Figure 12.** Synthetic spectrum fitting analysis for Al abundance determinations of AR Aur (P) and AR Aur (S) based on (a) Al I 3944, (b) Al I 3961, and (c) Al II 4663. The wavelength positions of the relevant Al lines are shown by vertical dashed lines. The scale of $F_\lambda/F_c$ indicated in the left axis is for AR Aur (P), while the spectrum for AR Aur (S) is shifted downward by 0.1. Otherwise, the same as in Fig. 7.

**Table 5.** Analysis results of AR Aur primary (P) and secondary (S).

|  |  | AR Aur (P) | AR Aur (S) |
|---|---|---|---|
| $T_{\mathrm{eff}}$ | (K) | 10950 | 10350 |
| $\log g$ | (dex) | 4.33 | 4.28 |
| $\xi$ | (km s$^{-1}$) | 1.0 | 1.6 |
| [Fe/H] | (dex) | +0.47 | +0.07 |
| $W_{3944}^{\mathrm{N}}$ | (mÅ) | (0.6) | 48.1 |
| $A_{3944}^{\mathrm{N}}$ | (dex) | (4.62) | 6.55 |
| $\Delta_{3944}$ | (dex) | +0.23 | +0.30 |
| $W_{3961}^{\mathrm{N}}$ | (mÅ) | (4.0) | 42.8 |
| $A_{3961}^{\mathrm{N}}$ | (dex) | (5.49) | 6.58 |
| $\Delta_{3961}$ | (dex) | +0.33 | +0.42 |
| $W_{4663}^{\mathrm{N}}$ | (mÅ) | (1.5) | 24.7 |
| $A_{4663}^{\mathrm{N}}$ | (dex) | (5.05) | 6.66 |
| $\Delta_{4663}$ | (dex) | +0.02 | +0.03 |

The parenthesized data derived for AR Aur (P) are subject to large uncertainties (because the line is considerably weak and barely detectable) and thus unreliable.

# Temporary capture of a small body into a geocentric orbit

## O. Bazyey[1,2] , A. Tokovenko[3] and V. Troianskyi[1,4]

[1] *Department of Physics and Astronomy FMPIT of Odesa I. I. Mechnykov National University, Pastera Street 42, 65082 Odesa, Ukraine (E-mail: o.bazyey@onu.edu.ua)*

[2] *Department of Mathematics, Physics and Astronomy, Odesa National Maritime University, Mechnykov Street 34, 65029 Odesa, Ukraine*

[3] *Astronomical Observatory of Odesa I. I. Mechnykov National University, Marazliivska 1v, 65014 Odesa, Ukraine*

[4] *Department of Physics and Methods of Teaching, Faculty of Physics and Technology, Vasyl Stefanyk Precarpathian National University, Shevchenko Street 57, 76000 Ivano-Frankivsk, Ukraine*

**Abstract.** The radius of the Earths activity sphere relative to the Sun is more than 900,000 km. New asteroids whose orbits intersect this sphere have been discovered every year. It would appear reasonable that under certain conditions of an asteroids approach to the Earth, it can be captured into a geocentric orbit. Using the method for a numerical simulation of test point masses in the gravitational fields of the Sun and major planets, we determined some orbital elements of the asteroids, which are most likely to be temporarily captured into geocentric orbits.

We came to the conclusion that semi-major axes of these orbits take values close to 0.97 au and 1.03 au. Hence, the heliocentric speed during rapprochement with the Earth should be close to $30.2 \, \mathrm{km \, s^{-1}}$ and $29.2 \, \mathrm{km \, s^{-1}}$, respectively.

We found that the most probable time for the existence of the asteroid in the Earth orbit is about 90-110 days; it can also be up to 180-200 days. But if an asteroid remains in the Earth orbit for more than 5 years, $\frac{3}{4}$ of such celestial bodies collide with the Earth.

**Key words:** Minor planets, asteroids: general – Methods: numerical

## 1. Introduction

The recorded passage of a small body over North America on 9 February 1913 initiated the study of the objects temporarily captured by the Earth-Moon system. A subsequent analysis of the orbit of the asteroid in the studies by Denning (1916) showed that the object was moving in a near-Earth orbit.

From the second half of the $XX$ century onward, the problem of temporary capture of asteroids into geocentric orbits has been the subject of many studies, like Baker (1958), Cassidy et al. (1965) and Cline (1979). The authors investigated the origin of temporarily captured asteroids, their orbital evolution, the possibility of collisions with the Earth, and the dynamic characteristics, such as velocity, total energy, and angular momentum. It has been found that for the temporary capture, the relative speed and the relative position of the asteroid near the Earth in the Sun's gravitational field must satisfy certain conditions. Our numerical research is dedicated to studying these conditions. The discovery of asteroid 2006 RH120 on 14 February 2006 sustained claims of the existence of other Earths moons temporarily captured by the Earth-Moon system. According to the computed orbital elements at the instant of the asteroids capture, it was moving along the heliocentric trajectory close to the Earths orbit. Having approached the Earth, the asteroid went into a geocentric orbit and stayed there from September 2006 to June 2007 (Kwiatkowski et al., 2009). Being Earths second known temporary natural satellite, or minimoon, asteroid 2020 CD3 (Fedorets et al., 2020).

This study aims to estimate certain characteristics of a small bodys temporary capture into a near-Earth orbit, namely the geocentric velocity, momentum, total energy before and after the capture, distribution of orbital elements, and a typical lifetime of the captured body in the near-Earth orbit.

We propose to use the change of the asteroid's angular momentum relative to the Earth as a criterion for its transition into the Earth orbit.

## 2. Numerical model

In the course of this study we developed a numerical model of the motion of a small celestial body in the Solar System. This model accounts for the perturbations by the main planets, Pluto and Moon, as well as light pressure and perturbation due to the second zonal harmonic in geopotential on the motion of the investigated small body.

In accordance with IAU resolution[1], the Solar System has 8 major planets, satisfying the conditions: (a) is in an orbit around the Sun, (b) has a sufficient mass for its self-gravity to overcome rigid body forces so that it assumes a hydrostatic equilibrium shape, and (c) has cleared its neighborhood around its orbit.

We do not take into account the Yarkovsky effect, since the magnitude and direction of the jet moment depend on the speed and the physical properties of the test particle surface.

The differential equations of motion of a small body were solved in Cartesian coordinates with numerical integration by the Everhart $15^{th}$-order method with an automatic step-size control (Everhart, 1974; Bazey & Kara, 2009):

---

[1] https://www.iau.org/static/resolutions/Resolution_GA26-5-6.pdf

$$\frac{d^2\overrightarrow{r_i}}{dt^2} + k^2(m_0 + m_i)\frac{\overrightarrow{r_i}}{r_i^3} = -k^2 \sum_{j=1}^{10} m_i \frac{\overrightarrow{r_i}-\overrightarrow{r_j}}{r_{ji}^3}$$
$$-k^2 \sum_{j=1}^{10} m_j \frac{\overrightarrow{r_j}}{r_{j0}^3} + \frac{\partial U}{\partial \overrightarrow{r}} + k^2 m_0 \beta \frac{\overrightarrow{r_i}}{r_i^3}, \quad i \neq j. \tag{1}$$

$$\begin{cases} \frac{\partial U}{\partial \overrightarrow{r}}\Big|_x = -\frac{3k^2 m_3 R_3^2}{2r^7} J_2 x(x^2 + y^2 - 4z^2), \\ \frac{\partial U}{\partial \overrightarrow{r}}\Big|_y = -\frac{3k^2 m_3 R_3^2}{2r^7} J_2 y(x^2 + y^2 - 4z^2), \\ \frac{\partial U}{\partial \overrightarrow{r}}\Big|_z = -\frac{3k^2 m_3 R_3^2}{2r^7} J_2 z(3(x^2 + y^2) - 2z^2). \end{cases} \tag{2}$$

Hereinafter, $\overrightarrow{r} = (x, y, z)$ is the position vector of the small body in the heliocentric system; $t$ is time, $k$ is the Gaussian gravitation constant, $m_0$ is the mass of the Sun, $m_i$ - the mass of the perturbing body: the eight major planets, Pluto and the Moon, $m_3$ - the mass of the Earth, $R_3$ - Earth's radius. On the right hand side of the equation, $\frac{\partial U}{\partial \overrightarrow{r}}$ is a disturbing acceleration due to the Earth's compression, $J_2$ is a coefficient of the second zonal harmonic of the geopotential in the expansion (Troianskyi, 2015). The last term on the right hand side accounts for the pressure of sunlight: $\beta = \frac{\kappa \theta P_0}{a_{gr}}$ - photogravitational reduction of the mass of the Sun, $\kappa$ - an optical coefficient of the small body surface, $P_0 = 0.0000045606 \,\text{N m}^{-2}$ - light pressure on the Earth's orbit; $\theta = \frac{A}{m_i} = \frac{3}{4R\rho}$ - a ballistic coefficient (windage)(Bazyey, 2014), $A$ - the area of the middle section, $R$ the radius of the small body, $\rho$ - the density of the small body (Troianskyi & Bazyey, 2015). $a_{gr}$ - the gravitational acceleration at the distance of 1 au from the Sun.

To account for the influence of the light pressure, the following parameters were assigned: $R = 100 \,\text{m}$, $m_i = 4.2 \times 10^9 \,\text{kg} = 2.1 \times 10^{-21} \, m_0$, $\rho = 1000 \,\text{kg m}^{-3}$, $\theta = 7.5 \times 10^{-6} \,\text{m}^2 \,\text{kg}^{-1}$, $a_{gr} = 5.9 \times 10^{-3} \,\text{m s}^{-2}$, $\kappa = 1$ (Troianskyi & Bazyey, 2018; Troianskyi et al., 2023).

To minimize integration errors and optimize the computation speed, calculations of the positions of major planets, Pluto and Moon, were eliminated from the integration process. Their orbital position vectors were taken from the numerical theory DE405[2] and used in the differential equations of motion at each integration step. In fact, this method is equivalent to the decomposition process of integration into single steps, when in each step the position and velocity of all celestial bodies, except our test body, are assigned initial values from DE405 theory. In other words, it makes no sense to reintegrate the equations of motion of the major planets, Pluto and Moon, when this is done with high precision in numerical theory of the Solar System.

---

[2] https://ssd.jpl.nasa.gov/planets/eph_export.html

## 3. Initial conditions

The subject of this study was a family of orbits of test small bodies. Their heliocentric position vectors were generated in a random manner. To estimate the conditions of temporary captures of small bodies into near-Earth orbits we generated 1.5 million initial state vectors.

To integrate the trajectory of motion we selected only those state vectors which met a series of conditions, in particular:

– the semi-major axis of a test small body should lie in the range from 0.87 au to 1.5 au;

– the orbital eccentricity ($e$) ranges from 0.0 to 0.12;

– the orbital inclination to the ecliptic ($i$) ranges from 2.5° to 2.5° (or from 20.93° to 25.93° to the celestial equator);

– the epoch is within the time interval of 19 years (Fotheringham, 1924);

– the longitude of ascending node ($\Omega$), argument of perihelion ($\omega$) and mean anomaly at the epoch were evenly distributed over the interval $2\pi$.

These initial conditions are selected on the basis of the study of Granvik et al. (2012). A 19-year period is used to eliminate the influence with rotation of the Lunar orbit.
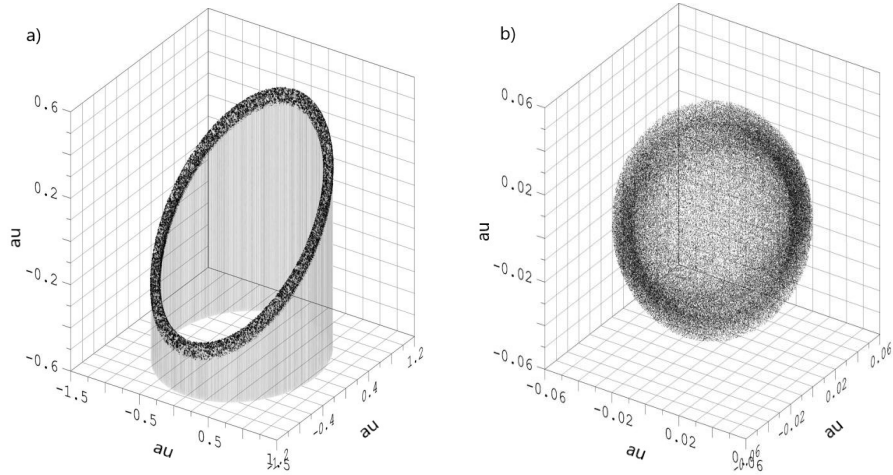


**Figure 1.** (a) Distribution of the initial conditions in the heliocentric system; (b) Distribution of the initial conditions in the geocentric system.

From the obtained range of small bodys initial conditions, the integration involved only those position vectors for which:

1) the geocentric distance at the start of integration was within the range of 0.04 au - 0.05 au;

2) the geocentric velocity of the object was smaller than its escape velocity at the same geocentric distance;

3) the angle between the geocentric direction and geocentric velocity vectors was smaller than 130° (Granvik et al., 2012).

The graphs for distribution of the initial conditions in the heliocentric and geocentric systems are presented below (see Fig. 1).

## 4. Definition of temporary capture

To determine whether a small body is the object captured into the Earth orbit or not, we used the following criteria:

1) the geocentric distance at the instant of the capture is smaller than three radii of the Hill sphere for the Earth ($\sim 0.03$ au; Kary & Dones (1996));

2) the number of full revolutions around the Earth is more than 1.
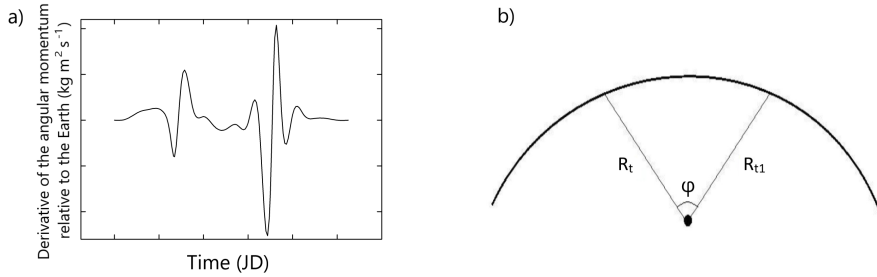


**Figure 2.** (a) A typical change in the angular momentum relative to the Earth of the small body temporarily captured into a geocentric orbit; (b) The angle between two position vectors of the small body in the geocentric orbit at the instants of time $t$ and $t_1$.

To determine the instant of transition of a small body from the heliocentric orbit to the geocentric orbit, and then back, we used the derivative of the angular momentum of the small body relative to the Earth (Fig. 2, (a)). The ordinate axis shows this derivative, measured in $(\mathrm{kg\,m^2\,s^{-1}})$, without values. For each

small body these values vary considerably, but there is always a very similar intermittent character of the curve (Fedorets et al., 2019).

We suggest interpreting such a stepwise change of this value as the transition of a small body from one orbit to another, that is, to define it as the instant of the capture of a small body by the Earth. Variation in the angular momentum of the small body can only be associated with the gravitational interaction with the Earth, such as the exchange of this value with the planet. As we know, this definition of transition into a geocentric orbit has not been previously introduced.

However, while such an exchange is not significant for the Earth because of a huge difference in the masses of celestial bodies, for a small body it means being temporarily captured into a near-Earth orbit.

The number of revolutions of a test small body around the Earth was determined by the angle between the position vector at the instant of capture (which corresponds to time $t$) and the position vector at the instant of the bodys return to the heliocentric orbit (which corresponds to time $t_1$), (Fig. 2,(b)).

## 5. Results

By substituting the obtained state vectors into the motion model, we observed the orbital evolution of test small bodies. The computation of the temporary capture parameters was started at the instant of their transition into geocentric orbits.

The instant of the integration end was not explicitly given. In case of a small bodys transition into a geocentric orbit, the instant of its return into the heliocentric orbit was reckoned as the instant of the integration end. Otherwise, the upper limit of the validity of the DE405 numerical model, the $20^{th}$ of February 2201, was taken as the end-time integration.
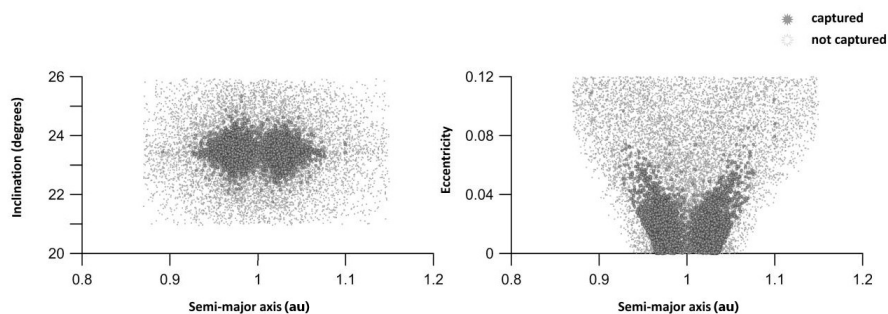


**Figure 3.** The interdependency between heliocentric orbital elements of the investigated small bodies.

Integrating the motion equations of the population of test small bodies resulted in the following: 14.4% of 1.5 million small bodies temporarily went into geocentric orbits, while 0.35% of them completed at least one revolution around the Earth. The small bodies which were also captured into geocentric orbits, but did not complete even one revolution around the Earth, were called transit ones.

The interdependencies between the orbital elements of captured and not-captured small bodies are presented below. The upper graph in Fig. 3 shows the orbital inclination toward the equator.

Based on the dependencies obtained, it is possible to unambiguously determine orbital elements for which the probability of a body being temporarily captured in a geocentric orbit is highest (Table 1).

**Table 1.** The limits of orbital elements for the captured small bodies. *Plane of the celestial equator.

|     | $a$, (au) | $e$  | $i^*$, (deg) | $\omega$, (deg) | $\Omega$, (deg) |
|-----|-----------|------|--------------|-----------------|-----------------|
| Min | 0.89      | 0    | 21.75        | 0               | 0               |
| Max | 1.10      | 0.11 | 25.73        | 360             | 360             |

The heliocentric velocity is the next dynamic characteristic to be discussed.
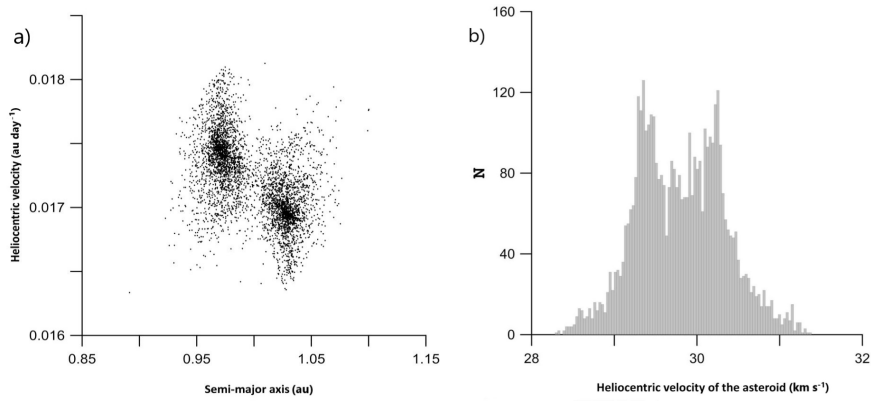


**Figure 4.** (a) The dependence of the heliocentric velocity of the captured particles on the semi-major axis of their orbit; (b) Distribution of heliocentric velocities of the captured particles.

As it follows from Figs. 4 (a), (b), the capture of a small body in the Earth's orbit is most likely when the heliocentric velocity lies between $29.2\,\mathrm{km\,s^{-1}}$ and $30.2\,\mathrm{km\,s^{-1}}$, while it is least probable when the semi-major axis of the test body and its heliocentric velocity are close to those of the Earth or, in other words, for bodies in orbits similar to the Earths one. With regard to the Earth moving at an average speed of $29.8\,\mathrm{km\,s^{-1}}$, the heliocentric velocity of such a small body does not exceed $0.6\,\mathrm{km\,s^{-1}}$. A temporary capture is most likely to occur at such low speeds due to the insignificance of the mass of the Earth relative to the Sun mass. In the case of collision with the Earth, speed's possible values can vary significantly.

The next dynamic characteristic studied was the lifetime of a captured small body in a geocentric orbit.
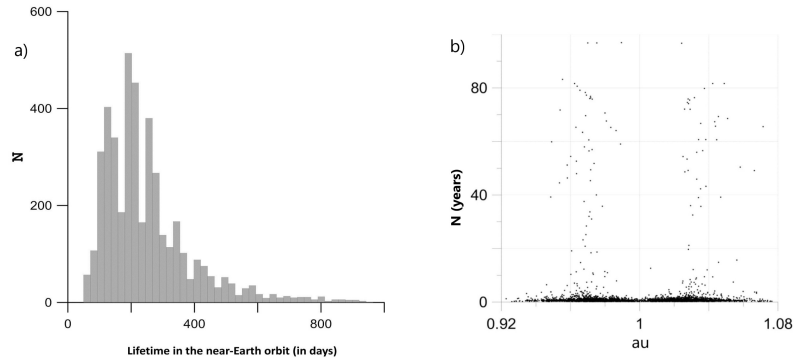


**Figure 5.** (a) Lifetime of a small body captured into a geocentric orbit; (b) Dependence of a small bodys lifetime on the semi-major axis of its orbit.

As it can be seen in Fig. 5 (a), the most probable lifetime in a geocentric orbit for small bodies that complete at least one revolution around the Earth is about 90-110 days. It can also be up to 180-200 days.

An equally interesting conclusion can be drawn upon considering the dependence of the semi-major axis of the captured small bodys orbit on its lifetime in that orbit.

As it follows from the graph, there are such values of the semi-major axes of the temporarily captured small bodies within the range of which the capture for an extended time span lasting for decades is possible. Such a capture is most likely to occur when the semi-major axis is close to $0.97\,\mathrm{au}$ and $1.03\,\mathrm{au}$ (see Fig. 5,(b)).

While simulating, we also obtained orbits of the small bodies which collide with the Earth. Among 1.5 million model orbits, we received 119 collisions.

It is interesting that 75% of the total number of captured long-lived objects (with the lifetime of a captured object in a geocentric orbit of 5-100 years) are accounted for by objects in collisional orbits.

## 6. Conclusions

The results of our simulation re-indicate the importance of the study of such objects as small bodies temporarily captured into geocentric orbits.

In the course of the numerical experiment, it was shown that small bodies moving along trajectories that are tangent to the Earth's orbit are most likely to be temporarily captured into near-Earth orbits. Most probable is the temporary capture of small bodies whose semi-major axis of the orbit is close to 0.97 au and 1.03 au. The probability of a small body being temporarily captured is least probable if the semi-major axis of its orbit is close to the semi-major axis of the Earths orbit.

Small bodies whose semi-major axes are close to 0.97 au and 1.03 au have the longest lifetime (up to 100 years) in the near-Earth trajectories.

It is necessary to take into account that an extended stay of a small body in a geocentric orbit increases the risk of its approaching to the orbits of artificial-Earth satellites, which may lead to their collisions.

The results obtained define the limits of the heliocentric orbital elements and the geocentric velocity for which a small bodys temporary capture into a near-Earth orbit is the most probable.

Thus we can suppose that for a temporary capture of an asteroid on the near-earth orbit, its heliocentric orbit must come liken the Earth orbits under for impact of different perturbations. Simple intersection and convergence of the orbits are not enough.

Perhaps this will determine among the known near-Earth asteroids, likely candidates for the temporary capture of the future, or to find asteroids that were captured in the past by the Earth.

## References

Baker, Robert M. L., J., Ephemeral Natural Satellites of the Earth. 1958, *Science*, **128**, 1211, DOI: 10.1126/science.128.3333.1211

Bazey, A. A. & Kara, I. V., Using of Everhart's method of 15, 17, 19 and 21st-order for computation of celestial bodies' trajectories in the circumplanetary space. 2009, *Astronomical School's Report*, **6**, 155, DOI: 10.18372/2411-6602.06.2155

Bazey, A. A., The Simulation of the Orbital Evolution of a Passive High-Orbit Fragment with Large Surface Area. 2014, *Odessa Astronomical Publ.*, **27**, 108, DOI: 10.48550/arXiv.1404.4570

Cassidy, W. A., Villar, L. M., Bunch, T. E., Kohman, T. P., & Milton, D. J., Meteorites and Craters of Campo del Cielo, Argentina. 1965, *Science*, **149**, 1055, DOI: 10.1126/science.149.3688.1055

Cline, J. K., Satellite Aided Capture. 1979, *Celestial Mechanics*, **19**, 405, DOI: 10.1007/BF01231017

Denning, W. F., The Remarkable Meteors of February 9, 1913. 1916, *Nature*, **97**, 181, DOI: 10.1038/097181b0

Everhart, E., Implicit Single-Sequence Methods for Integrating Orbits. 1974, *Celestial Mechanics*, **10**, 35, DOI: 10.1007/BF01261877

Fedorets, G., Granvik, M., Jones, L., Jurić, M., & Jedicke, R., Discovering minimoons with LSST. 2019, in *EPSC-DPS Joint Meeting 2019*, EPSC–DPS2019–1336

Fedorets, G., Micheli, M., Jedicke, R., et al., Establishing Earth's Minimoon Population through Characterization of Asteroid 2020 CD$_3$. 2020, *Astronomical Journal*, **160**, 277, DOI: 10.3847/1538-3881/abc3bc

Fotheringham, J. K., Metonic and Callippic cycles, The. 1924, *Monthly Notices of the RAS*, **84**, 383, DOI: 10.1093/mnras/84.5.383

Granvik, M., Vaubaillon, J., & Jedicke, R., The population of natural Earth satellites. 2012, *Icarus*, **218**, 262, DOI: 10.1016/j.icarus.2011.12.003

Kary, D. M. & Dones, L., Capture Statistics of Short-Period Comets: Implications for Comet D/Shoemaker-Levy 9. 1996, *Icarus*, **121**, 207, DOI: 10.1006/icar.1996.0082

Kwiatkowski, T., Kryszczyńska, A., Polińska, M., et al., Photometry of 2006 RH{120}: an asteroid temporary captured into a geocentric orbit. 2009, *Astronomy and Astrophysics*, **495**, 967, DOI: 10.1051/0004-6361:200810965

Troianskyi, V., Kankiewicz, P., & Oszkiewicz, D., Dynamical evolution of basaltic asteroids outside the Vesta family in the inner main belt. 2023, *Astronomy and Astrophysics*, **672**, A97, DOI: 10.1051/0004-6361/202245678

Troianskyi, V. V., Effect of Non-Sphericity of Gravitational Field of the Asteroid on the its Satellites Orbits Evolution. 2015, *Odessa Astronomical Publ.*, **28**, 299

Troianskyi, V. V. & Bazyey, O. A., The Solar-Radiation Pressure Effects on the Orbital Evolution of Asteroid Moons. 2015, *Odessa Astronomical Publ.*, **28**, 76

Troianskyi, V. V. & Bazyey, O. A., Numerical simulation of asteroid system dynamics. 2018, *Contrib. Astron. Obs. Skalnaté Pleso*, **48**, 356